Meteoritics & Planetary Science 40, Nr 12, 1835–1858 (2005)
Abstract available online at http://meteoritics.org

Spaceborne visible and thermal infrared lithologic mapping of impact-exposed subsurface lithologies at the Haughton impact structure, Devon Island, Canadian High Arctic: Applications to Mars

Livio L. TORNABENE[1*], Jeffrey E. MOERSCH[1], Gordon R. OSINSKI[2], Pascal LEE[3], and Shawn P. WRIGHT[4]

[1]Department of Earth and Planetary Sciences, University of Tennessee, Knoxville, Tennessee 37996–1410, USA
[2]Canadian Space Agency, John H. Chapman Space Centre, Longueuil, Quebec J3Y 8Y9, Canada
[3]Mars Institute, SETI Institute and NASA Ames Research Center, Moffett Field, California 94035, USA
[4]Department of Geological Sciences, Arizona State University, Tempe, Arizona 85287–6305, USA
[*]Corresponding author. E-mail: ltornabe@utk.edu

(Received 01 June 2004; revision accepted 22 July 2005)

Abstract–This study serves as a proof-of-concept for the technique of using visible-near infrared (VNIR), short-wavelength infrared (SWIR), and thermal infrared (TIR) spectroscopic observations to map impact-exposed subsurface lithologies and stratigraphy on Earth or Mars. The topmost layer, three subsurface layers and undisturbed outcrops of the target sequence exposed just 10 km to the northeast of the 23 km diameter Haughton impact structure (Devon Island, Nunavut, Canada) were mapped as distinct spectral units using Landsat 7 ETM+ (VNIR/SWIR) and ASTER (VNIR/SWIR/TIR) multispectral images. Spectral mapping was accomplished by using standard image contrast-stretching algorithms. Both spectral matching and deconvolution algorithms were applied to image-derived ASTER TIR emissivity spectra using spectra from a library of laboratory-measured spectra of minerals (Arizona State University) and whole-rocks (Ward's). These identifications were made without the use of a priori knowledge from the field (i.e., a "blind" analysis). The results from this analysis suggest a sequence of dolomitic rock (in the crater rim), limestone (wall), gypsum-rich carbonate (floor), and limestone again (central uplift). These matched compositions agree with the lithologic units and the pre-impact stratigraphic sequence as mapped during recent field studies of the Haughton impact structure by Osinski et al. (2005a). Further conformation of the identity of image-derived spectra was confirmed by matching these spectra with laboratory-measured spectra of samples collected from Haughton. The results from the "blind" remote sensing methods used here suggest that these techniques can also be used to understand subsurface lithologies on Mars, where ground truth knowledge may not be generally available.

INTRODUCTION

The visible-near infrared (VNIR; 0.4–1.4 μm), short-wavelength infrared (SWIR; 1.4–3 μm), and thermal infrared (TIR 7–14 μm) wavelength regions are the three primary regions that are used in current and planned reconnaissance mineral mapping of the terrestrial planets. Presently, spectra of the Martian surface are being collected at spatial scales that allow us to map small-scale (<1 km) compositional variations and geomorphic features. The thermal emission imaging system (THEMIS) on board the Mars Odyssey orbiter has 10 bands (8 of which are useful for compositional mapping of the Martian surface). THEMIS maps in the TIR with a spatial resolution of 100 m/pixel and has 5 bands in the VNIR with a spatial resolution of ~18 m/pixel (Christensen et al. 1999, 2003, 2004). THEMIS's predecessor, the 143-band thermal emission spectrometer (TES) on the Mars Global Surveyor orbiter (MGS), mapped global mineral and lithologic compositions at spatial resolution of approximately 3 × 6 km (Christensen et al. 1992, 1998, 2001). By combining the high spectral resolution of TES with the high spatial resolution of THEMIS, these two complementary instruments have been used to successfully identify small-scale compositional variation at the 100 meter-scale (Bandfield et al. 2004; Hamilton and Christensen 2005). In addition to THEMIS, spectral images of the Martian surface are currently being collected by the OMEGA instrument on board the European Space Agency's Mars Express. OMEGA possesses 352 contiguous bands in the VNIR and SWIR from 0.35 to 5.1 μm and has a spatial resolution ranging from 300 m to 5 km,

Table 1. Acronyms used in this paper.

Acronym	Meaning
ASTER	Advanced spaceborne thermal emission and reflection radiometer (Earth)
AVIRIS	Airborne visible/infrared spectrometer (Earth)
CRISM	Compact reconnaissance imaging spectrometer for Mars (Mars)
DCS	Decorrelation stretching
DEM	Digital elevation model
ETM+	Landsat7 enhanced thematic mapper plus (Earth)
IEM	Image derived end-member
MNF	Minimum noise fraction (a type of principle component analysis)
nDV	n-Dimensional visualizer
PPI	Pixel purity indexing
PPI-IEM	Refers to image-derived spectra selected by using a pixel purity indexing algorithm
RGB	Refers to the red, blue, and green channels that make up a color image
ROI	Region of interest
ROI	Refers to a user defined region of interest
SAM	Spectral angle mapper
SFF	Spectral feature fitting
SWIR	Short-wavelength infrared
SWIR-MNF	Refers to the RGB color-composite image generated by a minimum noise fraction transformation of ASTER SWIR bands 2, 1, and 6.
TES	Thermal emission spectrometer (Mars)
THEMIS	Thermal emission imaging system (Mars)
TIR	Thermal infrared
TIR-DCS	Refers to the RGB color-composite image generated by a decorrelation stretch of ASTER TIR bands 14, 12, and 10
VNIR	Visible-near infrared

depending on observation altitude (Bibring et al. 2005). In 2006, the 560-band VNIR and SWIR spectrometer known as the compact reconnaissance imaging spectrometer for Mars (CRISM), on board the Mars reconnaissance orbiter (MRO), will enable mineral and lithologic mapping of even smaller-scale features (18 m/pixel) and detect finer-detailed compositional variations than was previously possible (Murchie et al. 2003).

In preparation for working with such data sets from Mars, we can use multispectral imagers in Earth orbit as analogs. The two used in this study are the advanced spaceborne thermal emission and reflection radiometer (ASTER) and Landsat7 enhanced thematic mapper plus (ETM+). ASTER and ETM+ are reasonable analogs for THEMIS, OMEGA, and CRISM in that they have comparable spatial resolutions and cover at least 50% or more of the same spectral range.

The primary goal of this study is to lithologically map a terrestrial impact crater using ASTER and ETM+ data and, by analogy, to demonstrate the potential effectiveness of these types of remote sensing data sets for mapping Martian craters with THEMIS and CRISM. Impact cratering is the most ubiquitous geological process in the solar system and is common to all solid planetary bodies. Impact craters conveniently provide "windows" into planetary surfaces for mapping subsurface and shallow crustal materials, as demonstrated in similar studies of the Moon (Pieters 1982, 1991; Pieters et al. 1994, 1997; Tompkins 1998) and in situ on Mars by the Opportunity Mars exploration rover (Squyres et al. 2004). In addition to an investigation of lunar and Martian craters, studies of terrestrial craters have been successful in mapping subsurface lithologies at Meteor Crater, Arizona. Lithologies exposed in crater walls and ejecta blankets were successfully identified by a combination of remote and in situ methods (Garvin et al. 1992; Ramsey 2002; Wright 2003; Wright and Ramsey 2003).

Subsurface materials are exposed at the surface from a depth that is directly scaleable to the size of the crater (Housen et al. 1983; Schmidt and Housen 1987; Melosh 1989). This provides useful information for reconstructing approximate stratigraphic succession of the lithologies exposed. Complex craters are of particular interest for reconstructing a stratigraphic succession of subsurface and shallow crustal lithologies, because they excavate rocks and minerals from both the immediate subsurface and from the shallow crust. Complex crater morphologies form when the diameter of the transient cavity achieves a certain size upon which the crater can no longer sustain a simple bowl-shape morphology, which subsequently collapses. This transition is dependant primarily on gravity and the material strength, or rheology, of the target rocks. In addition to collapse and infilling during the formation of a complex crater, faulted terraces form along the crater wall, and a central peak or peak ring feature results from isostatic readjustment. Coherent lithologies originating from the midcrust level have been observed in field studies of the eroded central uplift of the Vredefort impact structure (e.g., Lana et al. 2003a, 2003b), which demonstrates the ability for complex craters to sample at least shallow crustal lithologies. Near-subsurface lithologies can also be observed as coherent rocks uplifted and exposed in the rim, the crater wall/terraces and, in some rare cases, within the ejecta blanket.

The effects of impact shock-induced changes in minerals and ejecta materials have gained further recognition in recent times in laboratory-collected spectra and image-derived spectra from both terrestrial and Martian data sets. In particular, shock effects in the collected hyperspectral TIR and VNIR spectra of quartz (Garvin et al. 1992), and of plagioclase and pyroxene have been documented (Johnson et al. 2002a, 2003; Johnson and Hörz 2003) and observed (Johnson et al. 2002b). Shocked plagioclase crystals were selected as end-members from the results of a deconvolution (i.e., unmixing) algorithm applied to TES-derived TIR spectra of the Martian surface. Although the effects of shock metamorphism on spectra for the major rock-forming silicate and non-silicate minerals have not been well documented, it is important to mention that such changes in multispectral data

(used here) are subtle and do not appear to affect broad compositional interpretations (Johnson et al. 2002b).

The 23 km (apparent) diameter Haughton impact structure was selected for this study based on four criteria: 1) the structure had to be of substantial diameter with respect to the spatial resolution of the imaging instrument(s); 2) the structure had to have moderately to well-preserved and discernible crater morphologic features (i.e., a rim, wall/terraces and central uplift); 3) there needed to be sparse vegetation and good exposure; and 4) the structure had to have been well-characterized, sampled, and geologically mapped, while offering reasonable access to the undisturbed target sequence stratigraphy for comparison. The diameter of Haughton ensures that a substantial depth is sampled and exposed for viewing by spaceborne remote sensing instruments. A crater tens of kilometers in diameter, like Haughton, has impact-excavated subsurface units that are still discernible even by the lowest spatial resolution data set used in this study (ASTER TIR, at 90 m/pixel). Haughton currently exists in a polar desert environment, which has kept the structure well preserved and prevents the growth of substantial vegetation cover. The well-preserved crater morphology facilitates mapping and interpretation of impact-exposed lithologic units, while the general lack of vegetation cover over Haughton facilitates a mineral and lithologic compositional assessment via remote sensing. Haughton formed within a sedimentary "layer-cake" stratigraphic sequence (referred to here as the "target sequence") with a tilt of 3–5° to the west-southwest, so that subsurface lithologies sampled by the impact event actually outcrop at the surface several kilometers to the east and northeast of the structure (Osinski 2004; Osinski et al. 2005a). This layout enables a direct comparison, by remote methods, of both impact-exposed subsurface units with corresponding outcropping units within the undisturbed target sequence within a single 60-km ASTER or 185-km ETM+ scene.

Table 1 is provided here as a reference for the numerous acronyms used in this paper, especially for the benefit of non-remote sensing oriented readers.

BACKGROUND

Geological Setting of the Haughton Impact Structure

The Haughton impact structure is a well-exposed and well-preserved complex crater centered at 75°22′N, 89°41′W on the western part of Devon Island, in the High Canadian Arctic Archipelago, Nunavut Territory. Haughton has an apparent diameter of 23 km based on recent mapping (Osinski and Spray 2005) and an age of 23.4 ± 1.0 Ma [Late Oligocene–Early Miocene; (Jessberger 1988). Originally mapped as a salt dome by (Greiner 1963) in the 1950s, Haughton was later proposed to be an impact structure by (Dence 1972), and subsequently, it was recognized as such based on the recognition of shatter cones (Robertson and Mason 1975) and the discovery of the impact generated high-pressure polymorph of quartz, coesite (Frisch and Thorsteinsson 1978). The target sequence at Haughton comprises a ~1880 m thick series of Lower Paleozoic sedimentary rocks of the Arctic Platform (Osinski et al. 2005a), overlying Precambrian metamorphic basement of the Canadian Shield (Fig. 1; map insert). Based on the apparent diameter of 23 km and recent scaling relationships for structural uplift, the maximum estimated excavation depth of the central uplift should be ~2,200 meters (Grieve and Pilkington 1996; Grieve and Therriault 2004). This estimate is similar to a previous estimate of ~1,970 meters (Grieve et al. 1981; Hajnal et al. 1988; Scott and Hajnal 1988), but is inconsistent with the most recent field estimate of ~1450 m for the central core (Osinski and Spray 2005).

Extensive re-mapping, combined with detailed petrological and analytical studies of pre-, syn-, and post-impact formations within and around the structure, has improved our understanding of the geology of Haughton (see Osinski et al. 2005 for an overview). As seen in Fig. 1a (or map insert), the major crater rim and wall rock units of Haughton consist mainly of the Ordovician-Silurian Middle and Lower Members of the Allen Bay Formation, which are comprised predominately of dolomite and limestone, respectively. However, exposures of the older Thumb Mountain, Bay Fiord and Eleanor River formations can be observed within the crater, and in undisturbed outcrop to the east and northeast of the structure. Shale from the Irene Bay Formation occurs in minor amounts within the faulted terrace blocks, as mapped in the field (Bischoff and Oskierski 1988; Osinski 2004), but most of the faulted terrace blocks consist predominantly of lower Allen Bay limestone, Thumb Mountain limestone and Bay Fiord gypsum (in descending order). The faulted crater rim consists predominantly of dolomite and limestone from different levels of the Allen Bay Formation. Limestones of the Thumb Mountain Formation outcrop in the inner crater around the outer edge of the central uplift in the southwest and east of the structure. The gypsum/anhydrite-bearing Bay Fiord Formation occurs predominantly in the east of the structure along the Haughton River valley, and as small blocks in the interior of the crater. Chert-bearing limestone of the Eleanor River Formation occur as centrally uplifted, kilometer-size blocks (>1050 m to <1300 m of uplift; Osinski et al. 2005a).

Haughton impact melt breccias, which line the inner basin of the structure (Fig. 1; map insert), consist of lithic clasts that are predominantly dolomite, with lesser amounts of limestone, shale, sandstone, gypsum/anhydrite, and lithologies from the crystalline basement (Redeker and Stöffler 1988; Osinski et al. 2005c). The groundmass (~50–60 vol%) consists of microcrystalline calcite (average ~20–25 vol%), silicate impact melt glass (average ~25–30 vol%) and anhydrite (highly variable; 0–60.5 vol%), with mineral

Table 2a. Landsat ETM+ and ASTER instrument characteristics.

Landsat 7 ETM+			ASTER		
Band	Center (μm)	Ground res. (m)	Band	Center (μm)	Ground res. (m)
1	0.485	30	1	0.556	15
2	0.560	30	2	0.661	15
3	0.660	30	3N	0.870	15
4	0.830	30	3B	0.870	30
Pan	0.52–0.90	15			
			4	1.656	30
5	1.650	30	5	2.167	30
7	2.215	30	6	2.209	30
			7	2.262	30
6	11.450	60	8	2.336	30
			9	2.400	30
			10	8.291	90
			11	8.634	90
			12	9.075	90
			13	10.657	90
			14	11.318	90

Table 2b. THEMIS, OMEGA, and CRISM instrument characteristics.

THEMIS			OMEGA			CRISM		
Band	Center (μm)	Ground res. (m)	Band	Center (μm)	Ground res.	Band	Center (μm)	Ground res. (m)
1[a]	0.425	19	1	~0.350	300 m–5 km	1	~0.400	18
2	0.540	19	.	.	.	.	.	.
3	0.654	19	.	.	.	.	.	.
4	0.749	19	.	.	.	.	.	.
5	0.860	19	.	.	.	.	.	.
			352	***~5.100***[b]	***300 m–5 km***	560	~4.050	18
1	**6.780**	**100**						
2	**6.780**	**100**						
3	**7.930**	**100**						
4	**8.560**	**100**						
5	**9.350**	**100**						
6	**10.210**	**100**						
7	**11.040**	**100**						
8	**11.790**	**100**						
9	**12.570**	**100**						
10	**14.880**	**100**						

[a]Plain text: VNIR; italics: SWIR; italics and bold: mid-IR; bold: TIR.
[b]5.1 μm is typically considered to be neither SWIR or TIR, but mid-IR.

and lithic clasts of various target lithologies (Osinski et al. 2005c).

The lake deposits of the post-impact Haughton Formation, which also occur in the inner basin, are varved and consist predominately of dolomitic sands, silts, and mud (Hickey et al. 1988). They may have once almost completely covered the impact melt breccia unit, but have been subsequently eroded away (Lee and Osinski 2005).

Non-geologic materials such as ice, snow, water clouds, and vegetation can obscure the ground and thereby affect lithologic mapping by remote sensing. These materials do exist in our scenes and, with the exception of vegetation, are addressed later in the Methods section.

Instrumentation

Table 2 provides a comparison of the wavelength coverage and spatial resolution of ETM+, ASTER, THEMIS, OMEGA and CRISM, which demonstrates the appropriateness of the two terrestrial instruments as analogs for present and future instruments designed for the remote sensing of Mars.

Although we recognize the 224 band airborne visible/infrared spectrometer (AVIRIS) with 20 m pixel resolution as a superior analog for both OMEGA and CRISM, there was no coverage available for Haughton at the time of this study. ETM+ is sufficient for the purposes of this study as it covers

approximately 50% of the wavelength range of both OMEGA and CRISM (Table 2). The ETM+ has been operational since April 1999, and consists of a whiskbroom-type multispectral imager with eight bands spanning visible to thermal infrared wavelengths. It is capable of scanning a cross-track swath, which creates a scene typically 185 km wide. For additional information on the Landsat7 ETM+ instrument see Goward et al. (2001).

The advanced spaceborne thermal emission and reflection radiometer (ASTER), operational since December 1999, is a 14-band, whiskbroom-type multispectral imager onboard the Earth observing system (EOS) TERRA platform. An ASTER scene covers an area approximately 60 × 60 km (for further information on the ASTER instrument, see Abrams [2000]). ASTER VNIR and SWIR bands cover similar wavelength ranges in common with OMEGA and CRISM; however, ongoing difficulties with a band-to-band "cross-talk" problem with the ASTER SWIR optics prevent a detailed spectral analysis in this wavelength region. The cross-talk issue arises from excess stray radiance reflecting off of the aluminum housing on the backside of filters adjacent to the detectors. This essentially results in band 4 radiance contaminating bands 5 and 9. This anomaly does not pose a problem for mapping spectral units. The cross-talk problem has an additive affect on bands 5 and 9 on all the spectra contained in the scene, while the remaining bands are truly representative of the surface properties. Therefore, spectral units can be mapped, but a positive match to library spectra is difficult due to modified values of band 5 and 9.

The cross-talk problem with the SWIR bands and the number of bands and positioning for the ETM+, which do not provide enough spectral resolution for the unique identifications of geologic materials, makes a full spectral analysis for these data sets not feasible. As a consequence, a full analysis of the ASTER TIR emissivity scene (as an analog for THEMIS TIR) (Table 1b.) will be emphasized in this study, while the other data sets will be used to map and constrain spectral/lithologic units.

On-Demand Data Products for Landsat 7 ETM+ and ASTER from EOS Data Gateway

ETM + and ASTER scenes were acquired from the EOS data gateway search engine and were selected based on three criteria: 1) time of year (to minimize the affects of ice and snow); 2) low cloud cover; and 3) coverage of Haughton and the surrounding area. The ETM+ Level 0R (L0R) scene LE7040007000021150 was acquired on July 29, 2000 at 18:01:48 at a sun elevation of 34.16° and meets all three criteria. The EOS data gateway generates a L1G product from the L0R, which includes both the necessary radiometric and geometric corrections.

An ASTER Level 1A (L1A) scene AST_L1A: 003.2003571915 was acquired on July 21, 2001 at 18:54:23, and also meets our all three of our criteria. The L1A data was processed by the Japanese ASTER ground data system (GDS) into a Level 1B (L1B) registered radiance with a product ID of: SC:AST_L1B:003.2017172817. This L1B radiance was then processed into higher level data products (Level 2B) via the EOS data gateway. These products include both the validated SWIR and VNIR surface reflectance (AST_07 v. 2.3) as one product, and the validated TIR surface emissivity (AST_05 v. 2.9). In addition to radiometric and systematic corrections, these data products are corrected for solar illumination effects, gaseous absorption, and molecular scattering. For more information on these products and the corrections applied to them, see http://asterweb.jpl.nasa.gov/content/03_data/01_Data_Products/SurfaceReflectance.pdf, http://asterweb.jpl.nasa.gov/content/03_data/01_Data_Products/Emissivity.pdf, Rowan et al. (2003), and Rowan and Mars (2003).

METHODS

ETM+ and ASTER SWIR and TIR data were pre-processed prior to applying mapping techniques to improve spectral mapping and matching results for "rock" surfaces associated with Haughton. Spectral reflectance data (Level 1G) from ETM+ scene LE7040007000021150 were processed as follows: 1) spatially subsetted the scene to only include the crater and most of the unaffected target sequence lithologies; and 2) applied a dark-object subtraction method, which offsets all pixel values in the scene so that shadowed pixels have a value of 0 (Chavez 1988). This correction minimizes spectral contributions from atmospheric scattering, thereby accentuating spectral contributions from surface materials. The correction is applied by recording the average digital number (DN) of shadowed areas in a grayscale image from the blue-wavelength band, and then offsetting the DN values of all the bands by the number. The correction value is taken from the blue-wavelength band, because scattering is most intense toward the blue wavelengths. ASTER Level 1B scene SC: AST_L1B:003.2017172817 was pre-processed into level 2 products (i.e., VNIR/SWIR reflectance and TIR emissivity) using the ASTER on-demand data gateway (http://edcimswww.cr.usgs.gov/pub/imswelcome). Areas in the scene covered by ice, snow, water, or clouds were removed from subsequent processing and mapping with an image mask.

These masks were created using threshold values ascertained from key bands sensitive to these substances. This substantially improved the results of subsequent mapping because the spectral variability in the unmasked portion of the scene primarily arises from differences in lithologic compositions. The total area covered by vegetation was so small that vegetation was not an issue.

Mapping and spectral analysis were all performed using the Environment for Visualizing Images (ENVI) software,

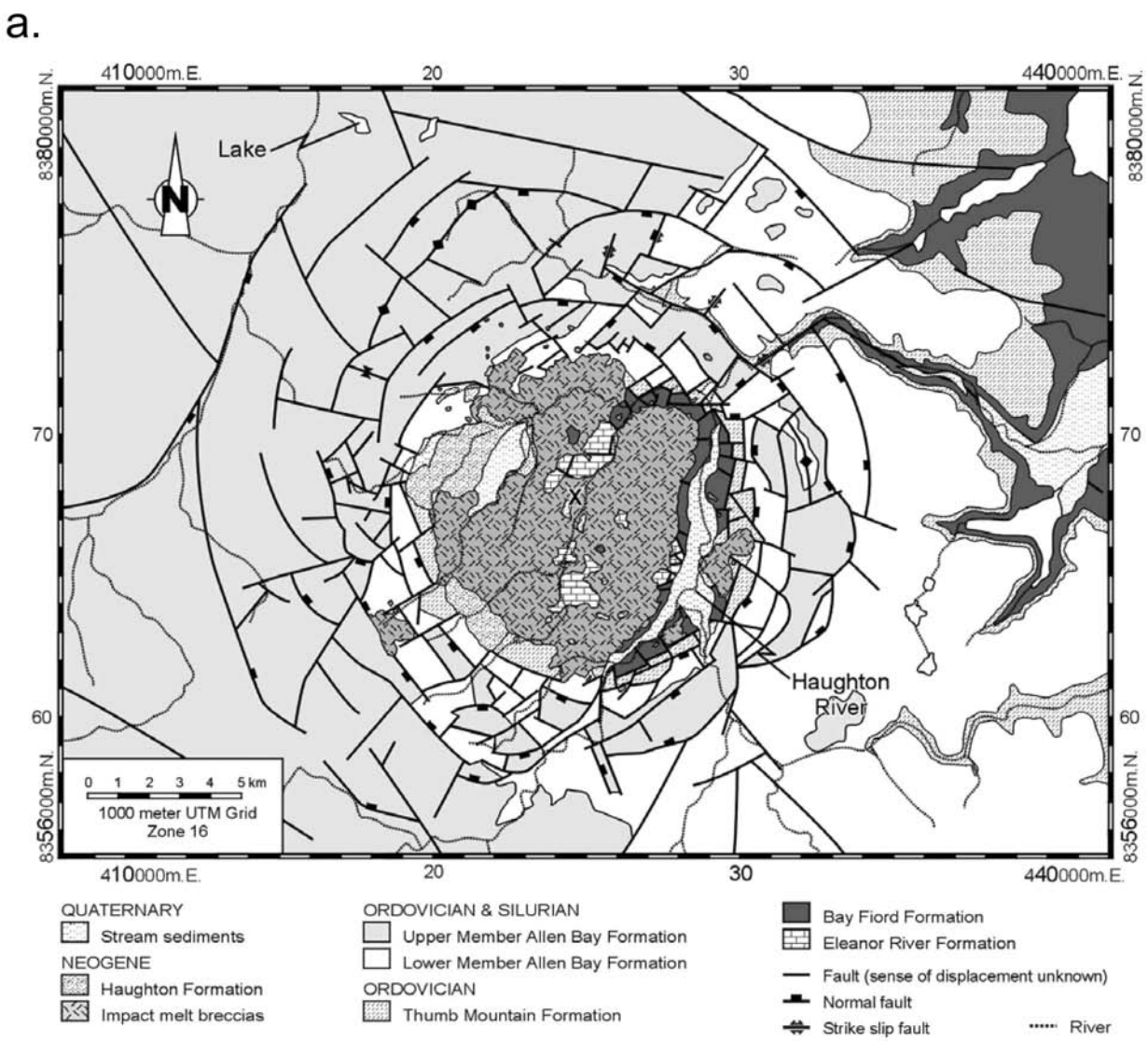

Fig. 1. a) A simplified geological map of the Haughton impact structure, after Osinski (2004). Lithological data beyond a 15 km radial distance from the center of the structure is from Thorsteinsson and Mayr (1987).

which is visual front-end for the interactive data language (IDL) programming language. The ETM+ and ASTER SWIR and TIR scenes were mapped using three commonly-used techniques that are useful for multispectral data to visually enhance spectral distinctness within the scene and thereby define "spectral units" (e.g., Figs. 2 and 3). The term "spectral unit" is used here to describe a contiguous area with discernible boundaries and bearing a relatively consistent color, or average spectrum, in any one of the processed images. Spectral units do not imply a pure mineral or rock type, although this could be possible, but may represent weathered surfaces, unconsolidated deposits, or non-geologic materials (e.g., vegetation, water, snow, ice or clouds, or even grain-size effects [most prominent in the TIR]).

The three mapping methods used here are: 1) decorrelation stretching (DCS); 2) a modified principle component analysis used to reduce noise called a minimum noise fraction (MNF) transform; and 3) band ratioing. These three methods are used here because they tend to sufficiently emphasize spectral variability in multispectral data sets. A DCS is a first-order mapping technique that enhances subtle spectral differences, but is limited to three different, user-selected bands (Gillespie et al. 1986). The original data values of the three selected bands are contrast-stretched and maximized to fill all the available color space, but the hues in the original red, green, and blue (RGB) combination are retained. A DCS was performed on bands 7-4-2 (not shown) from the ETM+ data set, 4-6-8 from the ASTER SWIR (Figs. 2a and 2c) and 14-12-10 from the ASTER TIR (Figs. 2b and 2d) (refer to Table 1b for band centers). These bands take advantage of the major absorption features and slope effects observed within each of the above scenes.

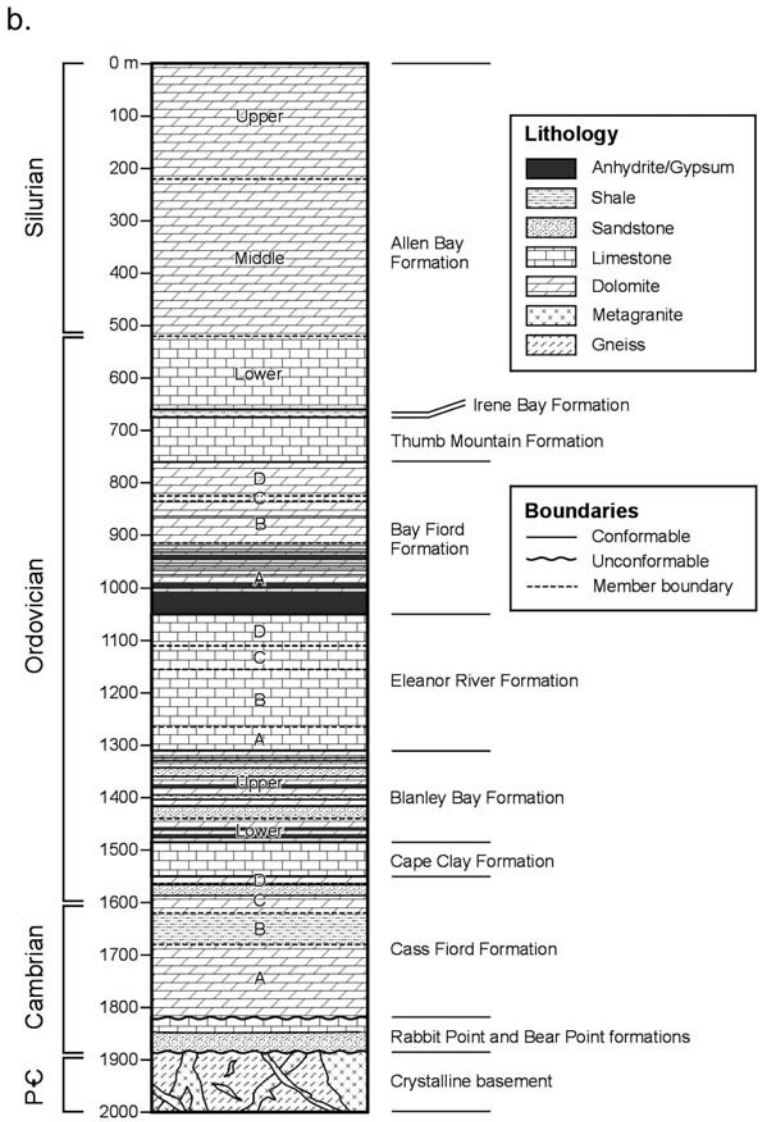

Fig. 1. *Continued*. b) Stratigraphic column showing the reconstructed target sequence at the Haughton impact structure compiled with data from Thorsteinsson and Mayr (1987) and modified by Osinski (2004).

An MNF was applied separately to the ETM+, ASTER SWIR reflectance, and the ASTER TIR emissivity data sets in order to maximize the spectral variation contained in all the available bands. This technique is unlike the DCS, which only uses 3 bands at a time. The MNF transform in ENVI 4.0 was modified after Green et al. (1988). The MNF classification, like a principle component (PC) routine, rotates the data into a new coordinate system and maximizes the variance of the data, but differs from a PC routine in that it segregates spatially correlated signal from noise (Boardman and Kruse 1994). Bands of the MNF-transformed data are ranked with the largest amount of spectral variance in the first band, and decreasing spectral variance with increasing band number until only noise and no coherent image remains. In multispectral data sets, the technique effectively isolates the predominant spectral components (i.e., distinct mineral/rock compositions) into separate bands. By discarding the higher-numbered noisy MNF bands and combining the lower bands into RGB, relatively noise-free spectral maps can be generated.

A band ratio image works by mathematically accentuating areas within a scene associated with the presence or absence of specific spectral absorption features (e.g., dividing a band positioned on the continuum by a band positioned for a known absorption feature). Band ratioing is most useful for multispectral imagery that lacks the spectral resolution needed for direct matching to library spectra (e.g., ETM+ data), and has been used extensively to map specific mineral groups in terrestrial remote sensing studies (Rowan and Mars 2003). The band ratioing mapping technique was applied to the ETM+ data set only because the ASTER SWIR suffers from the cross-talk problem and the ASTER TIR has

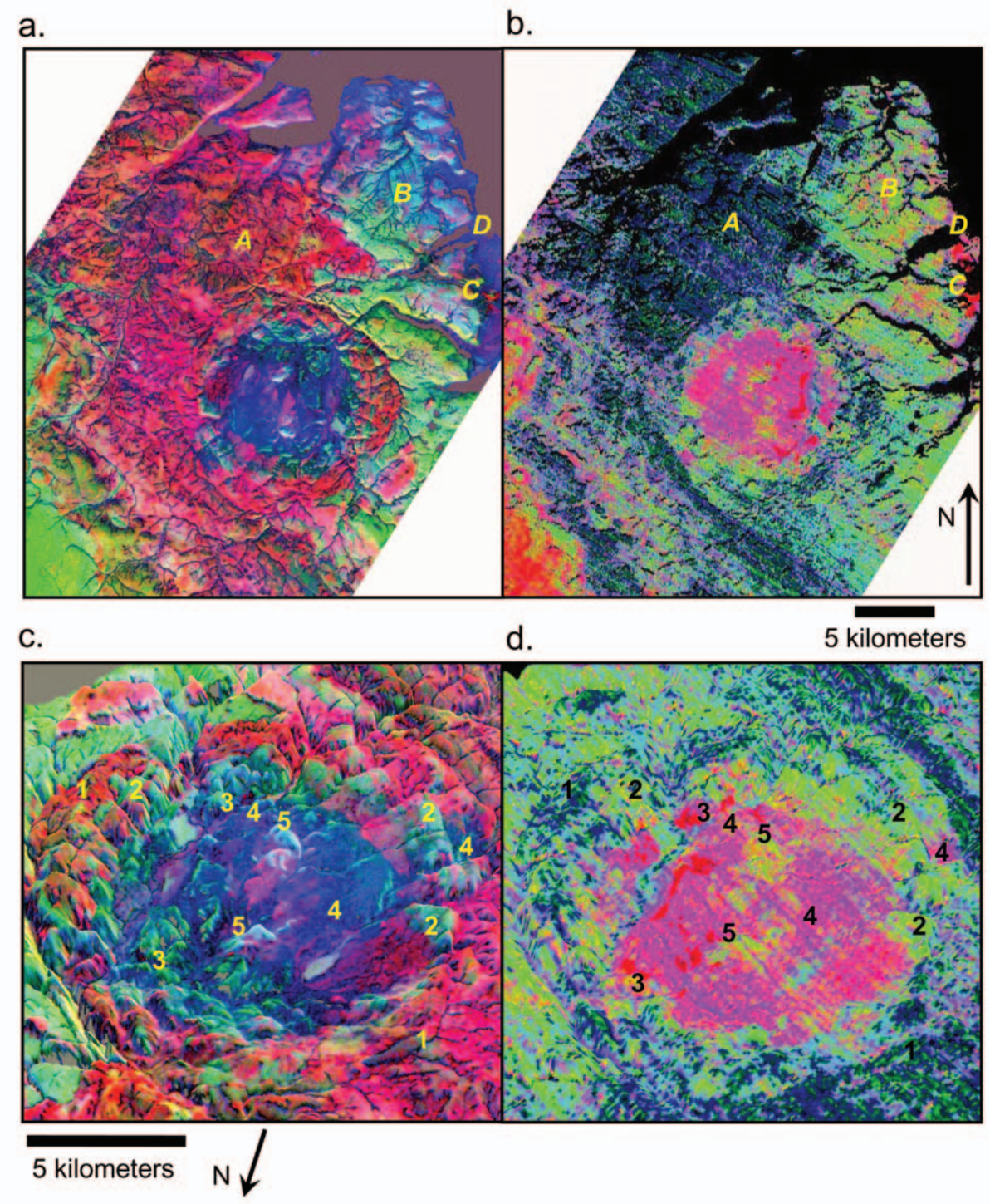

Fig. 2. a) ASTER SWIR minimum noise fraction (MNF) color composite image using MNF transformed bands 2, 1, and 6 in RGB. b) ASTER TIR decorrelation stretched (DCS) color composite image using bands 14, 12, and 10 in RGB of the Haughton impact structure and surrounding area. Capitalized letters A, B, and C denote three spectral units of the undisturbed target sequence. Unit D is not part of the undisturbed target sequence, but is noted as a unique spectral unit mapped within the scene. Gray and black areas in (a) and (b), respectively, are masked out areas of ice, snow, water, and clouds. c) A close-up of the ASTER SWIR MNF image from (a), and d) a close-up of the ASTER TIR DCS image in (b) superimposed on a 25 m resolution DEM with a vertical exaggeration of 10×. Numbers 1–5 denote crater ROI spectral units (ROI 1 = rim rock, 2 = wall rock, 3 = eastern floor, 4 = crater moat and 5 = central uplift). The colors representing the undisturbed target sequence units A, B, C correlate with the crater ROI units 1, 2, and 3. ROI unit 4 ("crater moat") is spectrally similar to Unit D. The DEM was provided by the Natural Resources of Canada.

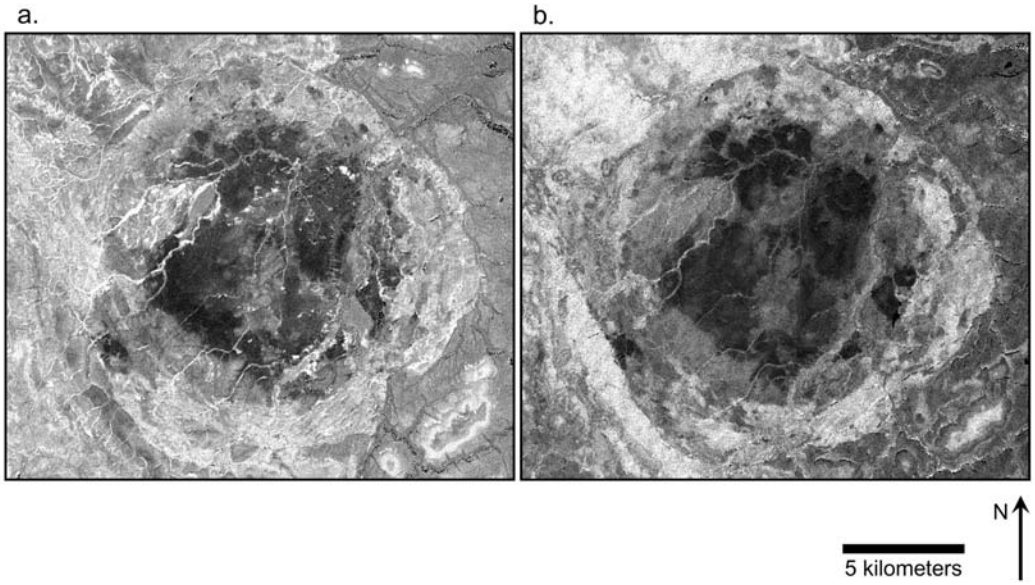

Fig. 3. ETM+ band ratio images with a 2% linear stretch. a) A band 5/band 7 image highlighting pixels that are strongly influenced by absorptions arising from the presence of carbonates, phyllosilicates, and hydrothermal alteration minerals. b) A band 3/band 2 image sensitive to the presence of any ferric iron (Fe^{3+})-bearing surface composition. Image (a) DN range: 1.067–1.365; image (b) DN range: 1.247–1.741.

both lower spatial resolution and signal-to-noise. Random noise is highly uncorrelated data having spurious data numbers (DN) so a ratio of any noise of this type will result in extreme values causing pixilation and striping. The band ratioing mapping technique works exceptionally well with the multispectral ETM+ data because it has both sufficient spatial resolution and a relatively high signal-to-noise ratio. Though ETM+ band ratio images are only suggestive of certain compositions, rather than being diagnostic, they are still useful for preliminary lithologic assessments prior to attempting any spectral matching techniques to a mineral or rock spectral library that contains hundreds of samples.

In order to further enhance the interpretability of all spectral maps created by the processing techniques above, each one was rendered into 3-D using a 25 m/pixel digital elevation model (DEM) of Haughton and the surrounding area (Natural Resources of Canada: http://www.nrcan-rncan.gc.ca/inter/index.html). These maps were then compared to one another to see if there were image-to-image correlations between the occurrences of spectral units and to discern if these units specifically coincided with crater morphologic features, such as the rim, wall, crater floor, and central uplift (thereby defining the shallowest [rim] to the deepest exposed units [central uplift]).

These mapping techniques do not in themselves rigorously attach specific mineral or lithologic compositions to each spectral unit. In order to make such assignments, both automated and manual methods were used to extract spectral end-members from the ASTER TIR emissivity product for matching to laboratory-measured spectra. Pixel purity index (PPI) and n-dimensional visualization (nDV) techniques are used in conjunction as an automated method to extract image spectral end-members (PPI-IEMs) (Boardman et al. 1995). The manual method used here simply averages all the pixels in a training area, referred to here as a region of interest (ROI). The PPI-IEMs and ROI-averaged spectra were then matched to library spectral end-members of whole-rock specimens from Ward's scientific (courtesy of Arizona State University, 2004) and minerals (Christensen et al. 2000a) using ENVI's spectral angle mapper (SAM) and spectral feature fitting (SFF) algorithms (Kruse et al. 1993). Note that the term "end-member," as used here, refers to a spectrum extracted from the unprocessed images, or from a mineral, rock, or sample spectral library. End-member spectra, like spectral units, may or may not represent pure minerals or rock-types, and do not necessarily refer to end-members in the sense of mineral solid-solution endmembers.

The PPI/nDV techniques extract spectra from the most "extreme" pixels within the scene, based on the assumption that these pixels are the purest end-members present, with all other pixels being composed of mixtures of these end-members. The PPI works by randomly reprojecting the n-dimensional data set (where n in the number of spectral bands) into a 2-D data plot for a user-determined number of iterations. The most extreme pixels at the vertices of the "data cloud" in each 2-D data plot are flagged. Each time a pixel is flagged, its PPI is incremented by one. The end-product of the PPI is an image, in which the value of each pixel corresponds to the number of times it was flagged over the number of iterations. In subsequent processing, only pixels with values above a user-defined threshold from this PPI image are used to choose end-members. The MNF values for these pixels are then plotted so that the analyst can rotate a 2-D projection of the data cloud from n-dimensions and extract image-derived

Table 3. Haughton impact structure spectral unit colors and matched compositions from SAM and SFF analyses.

Units	Location	MNF SWIR 2-1-6	DCS TIR 14-12-10	Spectral matches from spectral angle mapper (SAM) and spectral feature fitting (SFF)			
ROI | PPI	Impact-affected units	Color	Color	Ward's rocks	SAM (ROI | PPI)	ASU minerals	Score (ROI | PPI)
1 | 2	Rim	Magenta	Blue-green	Dolomitic LS[a]	0.991 | 0.988	Dolomite C28	0.990 | 0.990
2 | 3	Wall/terraces	Aqua	Yellowish green	Cherty LS	0.989 | 0.973	Calcite ML-C10	0.984 | 0.980
3 | 1	Eastern floor	Red	Red	Rock gypsum	0.980 | 0.978	Gypsum ML-S6	0.928 | 0.938
4 | 4	Crater moat	Blue	Pink	Graphite schist	0.996 | 0.995	Magnetite WAR-0384	0.995 | 0.992
5 | 3	Central uplift	Aqua	Yellowish green	Cherty LS	0.991 | 0.973	Calcite ML-C10	0.983 | 0.980
					SFF (ROI | PPI)		SFF (ROI | PPI)
2 | 3	Wall/terraces	Aqua	Yellowish green	Cherty LS	1.000 | 1.000		
3 | 1	Eastern floor	Red	Red	Rock anhydrite	0.902 | 0.891	Gypsum var. Alabaster	0.984 | 0.966
4 | 4	Crater moat	Blue	Pink	Cherty LS	1.000 | 1.000		
	Undisturbed units[b]						
A	*Surrounding plains*	*Magenta*	*Blue-green*	*Dolomitic LS*			
B	*East of impact structure*	*Aqua*	*Yellowish green*	*Cherty LS*			
C	*East and lower than B*	*Red*	*Red*	*Rock gypsum*			
D	*Lowest lying unit in valleys*	*Blue*	*Pink*	*Graphite schist*			
PPI 5	*Unit SW of Haughton*	*Reddish orange*	*Lime green*	*Siltstone*	*0.996*		

[a]LS denotes a limestone.

[b]Italic items pertain to the undisturbed target sequence or stratigraphically higher than the target sequence (e.g., PPI 5).

end-member spectra (PPI-IEMs) from the vertices of the data cloud.

The manual method used here consisted of defining regions of interest (ROIs) on the ASTER TIR emissivity product. The ROIs were based on spectral units that correlated between each of the spectral maps we generated (e.g., SWIR-MNF, TIR-DCS, and our ETM+ band ratio) and coincided with crater morphological features that were either excavated, uplifted, or exposed from different levels of the subsurface stratigraphy. The following crater ROI units were defined moving from the (presumably) shallowest subsurface to deepest uplifted unit (increasing unit number): 1) ROI unit 1("rim rock"), 2) ROI unit 2 ("wall rock"), 3) ROI unit 3 ("eastern floor"), 4) ROI unit 4 ("crater moat"), and 5) ROI unit 5 ("central uplift") (Table 3). The nomenclature used above was derived strictly from each unit's general morphological/spatial context within the crater and is not necessarily meant to be interpreted strictly in the genetic sense. These five crater ROI units were individually averaged into a single spectrum representative of that unit for spectral SAM and SFF analyses.

The SAM algorithm begins by representing an unknown spectrum as a n-dimensional vector, with the length of the vector in each dimension being the reflectance or emissivity (as appropriate) from each band in the spectrum. The SAM then compares the vector angle between each reference spectrum with the vector for the unknown spectrum in n-dimensional space. Any library reference spectrum that receives a SAM score of 1.000 for a given unknown spectrum is a perfect match (i.e., if the library of reference spectra is appropriate to the scene). Because the SAM results are highly dependant on the end-members contained in the input library, a score below 1.000 is typical. Therefore, we define the best-matched library reference spectrum for any given PPI-IEM or ROI-averaged spectrum with a score of 0.980 or greater. SFF was applied to suspect SAM matches below 0.980 to better constrain the identity of these spectra. The SFF algorithm works by removing the continuum for the unknown and library end-members, and then directly compares the absorption features that remain. Like the SAM class, the SFF returns a score of 1.000 for perfect matches. Table 3 reports the results from the SAM and SFF classification using the Arizona State University's (ASU) mineral spectral library (Christensen et al. 2000a) and a whole-rock library of Ward's scientific specimens (courtesy of ASU, 2004).

In order to further constrain the composition of each spectral unit, a spectral linear deconvolution algorithm (Ramsey 1996; Ramsey and Christensen 1998) was applied to a subset of the ASTER TIR emissivity product containing Haughton and the exposed undisturbed target sequence. Linear deconvolution (i.e., linear unmixing) of TIR spectra is possible because mineral or lithologic mixtures are linearly additive in the TIR (Thomson and Salisbury 1993; Ramsey 1996). Therefore, each pixel can be unmixed into its mineral or rock areal abundance. Each spectral library set, the PPI-derived IEMs, crater ROI-averaged spectra, and both the best whole-rock (Ward's) and the mineral (ASU) SAM matches for the PPI and ROI-averaged spectral end-members were used as inputs for the algorithm (Table 3; Fig. 5). PPI-IEM and ROI-averaged spectra are used here, as they have been successfully used in other studies towards deconvolving and mapping spectral units within the scene from which they were derived (Adams et al. 1993). A pure blackbody end-member was included in each of the four sets to allow the deconvolution algorithm to accommodate and model reductions, or increases, in spectral contrast in the unknown image spectra (from the scene) as compared to the library spectra used. Such reduction or increases in spectral contrast can result from the grain size effects, surface roughness, and degree of crystallinity or sample purity. By adding a positive or negative blackbody to the input spectra, the spectral contrast of the spectrum to be unmixed can be adjusted to match the contrast of the input reference library spectra.

The n-possible end-members used as an input for the deconvolution algorithm is mathematically limited to the n-bands of the instrument (Ramsey 1996). In the case of ASTER, the n-band value is five, which limits the number of input spectra for the algorithm to five or less. Five PPI image-derived end-members were chosen from the scene, and also five ROIs were selected (the maximum number allowable by the algorithm). The number chosen by the PPI/nDV method and the number of ROIs was not chosen to suit the algorithm. Five was the actual number of extremes in the PPI-derived data cloud and the number of spectral units in the scene that correlated with crater features. From over 100 end-members in both the rock and mineral libraries, the SAM classification was able to constrain the four (plus a blackbody) or five reference library spectral end-members, for each of the PPI-IEM or ROI-averaged spectra, required by the algorithm.

The results from all techniques described above were interpreted blindly, without making use of pre-existing field studies (e.g., maps, etc.) or ground truth data (i.e., hand specimen or field spectra). The purpose was to simulate remote sensing studies of Martian craters, for which little to no ground truth data are available. The results from our blind analysis were compared to a geologic map and stratigraphic column from the latest field observations derived from the first seven field campaigns of the NASA Haughton-Mars project (Osinski 2004; Osinski et al. 2004, 2005a, 2005b; Osinski and Spray 2005). Finally, PPI-IEM and ROI-averaged spectra were compared to spectra of Haughton samples as a final ground truth step.

RESULTS AND INTERPRETATIONS

Description of the Crater-Spectral Units and the Undisturbed Target Sequence

Color composite images created from different combinations of minimum noise fraction (MNF)-transformed

and decorrelation stretched (DCS)-transformed ASTER bands were used to manually identify ROIs associated with different spectral units that coincided with both crater morphological features and with the units of the undisturbed target sequence. Fig. 2 shows two of these types of images with exposed and uplifted crater ROI units denoted by a number and related undisturbed target sequence units bearing a letter designation that increases with descending order within the stratigraphic sequence from A to D, with A being related to ROI unit1, B to 2, etc. (Table 3). The two best color composite processed images were those that displayed the least noise and best revealed a clear correlation between spectral units and crater morphological features. These two images were created from a combination of SWIR MNF bands 2, 1, and 6 (Figs. 2a and 2c) and the DCS-enhanced ASTER TIR bands 14, 12, and 10 (Figs. 2b and 2d). These two maps will be discussed and referred to below as "SWIR-MNF" and "TIR-DCS."

ROI units are more difficult to discern in the TIR-DCS, but can be easily discriminated in the SWIR-MNF image. As a consequence, ROIs were identified in both images (Fig. 2) to facilitate extraction of spectra from the appropriate spectral units within the ASTER TIR emissivity data set. Gray pixels in the SWIR-MNF color composite images (Figs. 2a and 2c) indicate where a mask for non-geologic materials was applied. Although such a mask is not required for DCS processing, one was applied for consistency. The black pixels in the TIR-DCS images (Figs. 2b and 2d) indicate where the mask was applied for this image.

In Figs. 2a and 2c, the crater rim lithology has a magenta color in the SWIR-MNF (ROI unit 1 ["rim rock"]) and appears stratigraphically as the topmost, N-S trending unit sampled by the impact event (Unit A; best seen in Fig. 2a). These units correlate with dark blue-green pixels in the TIR-DCS (Figs. 2b and 2d). Unit A appears to conformably overlie Unit B (i.e., the aqua unit in the SWIR-MNF image and the yellowish green unit in the TIR-DCS image). Evidence for this stratigraphic succession can be seen to the northeast and southeast of the impact structure (Fig. 2a), where erosional mesas capped by Unit A (magenta) are underlain by the subordinate Unit B (aqua). The aqua pixels corresponding to outcrops within the crater walls, and although the same color is observed for centrally uplifted blocks (i.e., ROI unit 5), the aqua-colored pixels associated with outcrops within the wall or slumped terrace blocks are treated here as a separate unit (ROI unit 2 ["wall rock"]). This unit appears yellowish green in the TIR-DCS images (Figs. 2b and 2d).

Occurrences of isolated bright red pixels in both SWIR-MNF and TIR-DCS can be seen to the east-northeast of the crater (Unit C), which is interpreted as part of the undisturbed target sequence. Outcrops of this unit can be found within the northeast and southeast parts of the "crater moat" unit, and also around the more northern central uplift block. This unit is referred to as ROI unit 3 ("eastern floor").

The most obvious spectral unit associated with Haughton occupies the interior basin, or moat, of the Haughton impact structure and is dark blue in the SWIR-MNF or pink in the TIR-DCS. This particular spectral unit, referred to as ROI unit 4 ("crater moat"), also outcrops as a patch of material overlying the rim rock in the southwest region of Haughton. Additional occurrences of dark blue/pink pixels in these images can be seen as valley-fill and shoreline deposit materials to the north of Haughton (unit D).

ROI unit 5 ("central uplift") has the same color as ROI unit 2 ("wall rock") in both the SWIR-MNF and TIR-DCS combinations, suggesting that they have similar compositions. ROI unit 5 is defined separately from ROI unit 2 ("wall rock") because it occurs in association with what appear to be centrally uplifted blocks on the crater floor.

Spectral Analysis and Interpretation

Band ratio images constructed from ETM+ data were used to make compositional inferences about the spectral units defined above. Such inferences can be used to further constrain the best matches for PPI-IEM and ROI-averaged spectra from the results of the SAM and SFF classification (discussed below). The ETM+ band ratio images (Figs. 3a and 3b) only show spectral signatures related to gross lithologic differences (e.g., carbonate versus silicate) because of ETM+'s band placement and low spectral resolution. Two standard ETM+ band ratios (Drury 2001) were used: 1) a ratio of band 5 to band 7 (Fig. 3a), for carbonates, phyllosilicates and hydrothermally-altered deposits; and 2) a ratio of band 3 to band 2 (Fig. 3b), which produces an image sensitive to ferric iron (Fe^{3+}). The brightest pixels in the 5/7 image (Fig. 3a) are found near or within tributaries of the Haughton River, and as clustered, isolated spots within the crater floor and around the northern centrally-uplifted blocks. These pixels are interpreted to represent fluvial deposits that are possibly rich in phyllosilicates or carbonates. The brightest spots in this image associated with the eastern crater floor and around the central uplift in this image correlate well with the ROI unit 3 ("eastern floor"). This occurrence is interpreted as outcrops rich in carbonates, phyllosilicates or, specifically, sulfates (due to a stronger absorption in band 7 then is generally expected for carbonates and phyllosilicates).

The brightest pixels in the 3/2 band ratio image (Fig. 3b) are within the outcrops in the ROI unit 1 ("rim rock"), which stratigraphically overlies ROI unit 2 ("wall rock"), the darker, grayish unit to the east of Haughton. Examination of the average spectrum for both units reveals a weak absorption in band 7 suggesting that they may represent carbonates or phyllosilicates with ROI unit 1 representing a unit richer in Fe^{3+} than ROI unit 2.

PPI/nDV analysis of the entire ASTER TIR scene for Haughton, minus the pixels masked for ice, water, snow, and clouds yielded the five PPI-IEMs. Spectra from the five

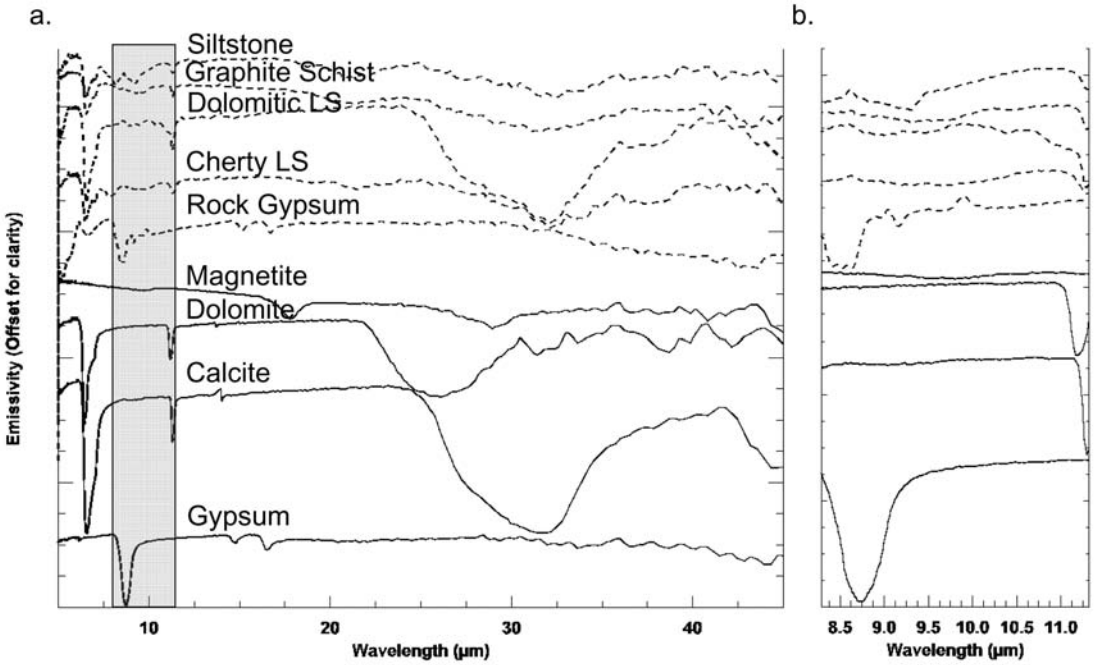

Fig. 4. Unconvolved TIR spectra collected by Arizona State University's Nicolet Nexus 670 spectrometer of whole-rock (Ward's = dashed) and mineral (ASU = solid) library spectral end-members. These two plots show the Ward's and ASU spectral matches for ASTER emissivity spectra extracted from the Haughton scene. a) Over the full spectral range and spectral resolution of the laboratory spectrometer. b) Over just the spectral range corresponding to ASTER's TIR channels (also shown as the shaded area in [a]). Spectra in both (a) and (b) are offset for clarity. Tick marks represent 0.125 and 0.05 emissivity values for (a) and (b), respectively.

manually defined crater ROI units closely match four out of the five PPI-IEM spectra. End-members chosen by the SAM and SFF algorithm for both PPI-IEM and ROI-averaged spectra are shown at their full-spectral resolutions in Fig. 4. These spectra are also shown in Figs. 5a–e convolved to THEMIS band passes (solid lines) and compared with both PPI-IEM and ROI-averaged spectral end-members (dashed lines). Even at ASTER TIR spectral resolution (5 bands), the PPI and crater ROI spectra can be assigned compositional labels by visually comparing them with mineral (ASU) and whole-rock (Ward's) library spectral end-members selected by SAM and SFF classification.

PPI-derived IEM#1 (Fig. 5a) has the deepest absorption feature in the scene with an average emissivity of 0.82 at ~8.63 μm. This end-member was derived from crater ROI unit 3 ("eastern floor") and the undisturbed country rock Unit C (Figs. 2a and 2b). Note the similarities between the main absorption features for the mean spectrum from both the PPI-derived IEM#1 spectrum and the manually-defined eastern floor unit (ROI unit 3) and the ASU Gypsum ML-S6 and the Ward's whole-rock gypsum end-members. The strong absorption feature at ~8.63 μm is consistent with the presence of gypsum ($CaSO_4 \times 2\ H_2O$), but the downward deflection at ~11.32 μm suggests that both PPI-IEM#1 and crater ROI unit 3 have spectral contributions attributed to the presence of carbonate. The sulfate interpretation of this unit is consistent with information gleaned from ETM+ band ratio images (above).

ROI unit 3 ("eastern floor") is interpreted to be a subsurface unit lying between ROI units 2 and 5. Outcrops of this unit in the undisturbed target sequence (Unit C) occur approximately at the same stratigraphic elevation as occurrences within Haughton, which can be seen in the DEM processed images (Figs. 2c and 2d). This suggests that the Haughton occurrence of this unit likely represents an impact-exposed subsurface unit. Occurrences of this unit around the northern central uplift block also suggest that this unit may have conformably overlain the unit exposed by the central uplift prior to the impact event. In addition, the placement of the unit can be correlated with its proper succession within the undisturbed target sequence (units A–C). Lithology unit C (red) appears subordinate to unit B (aqua or yellowish green) to the northeast of Haughton (Figs. 2a and 2b).

PPI-IEM#2 and ROI unit 1 (Fig. 5b) are identified as carbonates on the basis of a main absorption feature at ~11.32 μm. They also contain minor silicate absorptions (possibly quartz) around ~9.08 μm. The PPI-derived IEM#2 corresponds well to the manually-selected ROI unit 1 ("rim rock"). SAM classification results using the ASU and Ward's library suggested that Dolomite C28 and the dolomitic limestone end-members were the best matches for PPI-IEM#2 and ROI unit 1 ("rim rock"). Additional evidence that the carbonate forming this particular unit is dolomitic comes from the ETM+ band ratio 3/2 image (Fig. 3b). As previously described, ROI unit 1 ("rim rock") appears as a unit containing the brightest pixels in the band ratio 3/2 image,

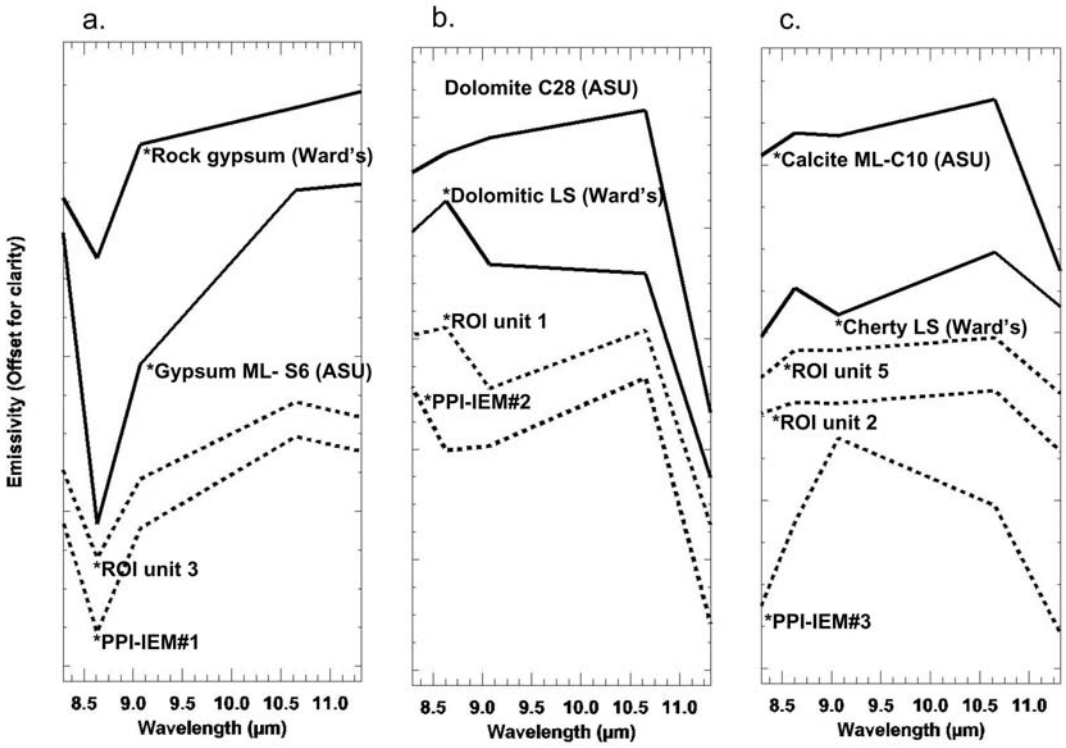

Fig. 5. A comparison of ASTER TIR image end-member (IEM) (solid lines) and ROI-averaged spectra (dashed lines) with the best-matching mineral and whole rock spectra from the ASU and Ward's spectral libraries derived from SAM and SFF classification. Library spectra were convolved to the ASTER TIR band passes (solid lines) for comparison. a) Average spectra for PPI-IEM#1 and crater ROI unit 3 ("eastern floor") compared to the spectra for Gypsum ML-S6 and rock gypsum. b) Average spectra for PPI-IEM#2 and crater ROI unit 1 ("rim rock") compared to the spectra for Dolomite C28 and a dolomitic limestone. c) Average spectra for PPI-IEM#3, crater ROI unit 2 ("wall rock") and crater ROI unit 5 ("central uplift") compared to the spectra for calcite ML-C10 and a cherty limestone.

which is sensitive to the presence of Fe^{3+}. Ferric iron preferentially substitutes more readily into a dolomite structure than into calcite, making ROI unit 1 brighter over the subordinate ROI unit 2 ("wall rock"). Siderite (ASU) and a siderite carbonatite (Ward's) were chosen as possible end-members by SAM classification, but were rejected as possible matches because of a lower (<0.98) SAM score and due to the fact that siderite rarely ever occurs in massive layered beds. This does not preclude that some minor siderite may contribute to the spectral signature of ROI unit 1, or PPI-IEM#2.

PPI-IEM#3 (Fig. 5c) pixels correlate with the position of both crater ROI unit 2 ("wall rock") and ROI unit 5 ("central uplift"). The main absorption feature for PPI-IEM#3 and both ROI spectra is located near ~11.32 μm. Both ROIs have minor absorption features near ~9.08 μm (possibly a quartz signature) but are difficult to discern. The SAM and SFF classification results for IEM#3, ROI unit 2 and ROI unit 5 suggests a cherty limestone (Ward's) and Calcite ML-C10 (ASU) as best matches. ROI unit 5 is interpreted as a separate unit derived from deeper sources than ROI unit 2, because it outcrops within centrally uplifted blocks and appears to be separated from ROI unit 2 by unit 3. Lithologies contained within central uplifts in complex craters have the deepest origins with respect to the pre-impact stratigraphy (e.g., Grieve et al. 1981).

Spectra derived from PPI-IEM#4 and ROI unit 4 ("crater moat") are almost identical (Fig. 5d). The SAM classification best match for these units using the Ward's and ASU spectral libraries were a graphite schist and Magnetite WAR-0384, respectively, neither of which appears to be consistent with the other lithologies identified (i.e., carbonates, evaporates, and silicates). However, if we compare the "crater moat" unit's average spectrum with either the first four PPI-IEMs or the four crater ROI-averaged spectra (Figs. 5a–c), each absorption feature in the "crater moat" spectrum can be easily explained as arising from mixing of these components. A slight deflection at ~8.63 μm can be explained by mixing some gypsum-rich component into the "crater moat" unit, and the absorptions at ~9.08 μm and ~11.32 could be from mixing in a quartz-rich component and carbonate-rich component, respectively. Identification of the exact mineral species of carbonates and silicates of the "Crater moat" unit is hampered by the unit's lack of spectral contrast (<0.98) (Fig. 5d). While we do not necessarily find the specific interpretation of the graphite schist correct, inspection of the full spectrum of this library sample (Fig. 4a) reveals that it has absorptions that are consistent with both carbonates (6.6, 11.3, 14 and a broad

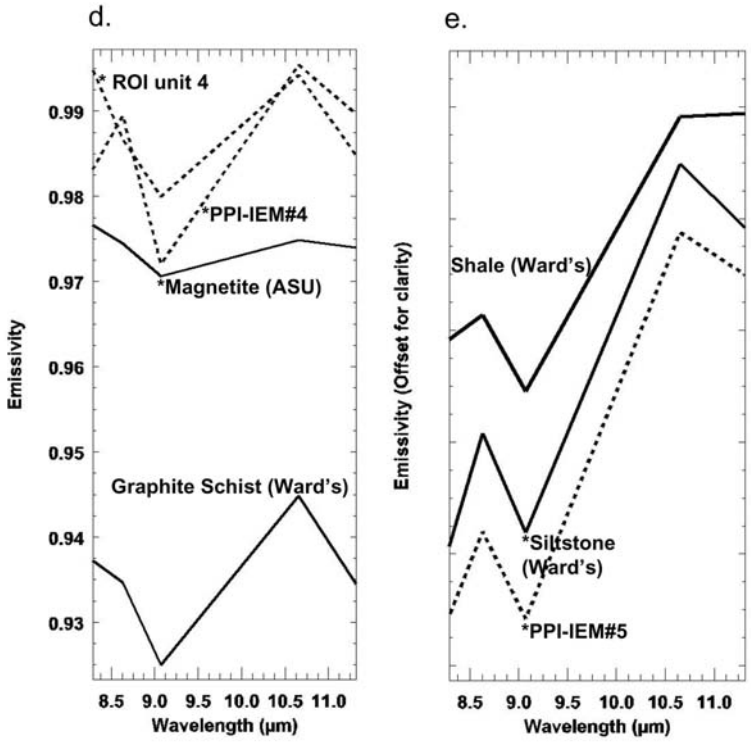

Fig. 5. *Continued*. A comparison of ASTER TIR image end-member (IEM) (solid lines) and ROI-averaged spectra (dashed lines) with the best-matching mineral and whole rock spectra from the ASU and Ward's spectral libraries derived from SAM and SFF classification. Library spectra were convolved to the ASTER TIR band passes (solid lines) for comparison. d) The average spectrum for PPI-IEM#4 compared to the spectra for shale and siltstone. e) The average spectrum for PPI-IEM#5 and crater ROI unit 4 ("crater moat") compared to the spectra for magnetite WAR-0384 and a graphite schist.

absorption around 32 μm) and silicates (8.6 and a broad absorption around 20.3 μm). To this extent, the match is likely to be valid with respect to some of the minerals representative in the graphite schist end-member because both carbonates and silicates are found in adjacent spectral units. However, in a lithologic sense, a graphite schist is neither consistent with the other lithologies present nor the inferred tectonic setting. With respect to ASTER TIR-derived spectra, the minor absorption features outlined above for the "crater moat" unit suggest that it possibly consists of a mixture of all four crater ROI units and possibly a quartz-rich component similar to PPI- IEM#4. Unfortunately, corroboration of this hypothesis using deconvolution analysis was not possible due to the low spectral contrast of the "crater moat" spectrum.

The PPI-selected pixels used to create the IEM#5 spectra (Fig. 5e) originate from an undefined spectral unit (reddish orange) well outside of the Haughton structure and the undisturbed target sequence, to the southwest of the impact structure (Fig. 2b). The spectrum for PPI-IEM#5 resembles the spectrum for pure quartz, but the SAM classification preferred a siltstone or shale from the Ward's spectral library. Quartz has a primary spectral absorption feature at ~9.08 μm. Absorptions at this wavelength can be seen in some of the ROI spectra, especially in the "rim rock" and the "crater moat" unit, suggesting some spectral contributions from quartz.

Table 4. Root mean square (RMS) statistics from the whole-image deconvolution of Haughton and surrounding terrain.

Spectral end-members	Min.	Max.	Mean	1σ Std. dev.
PPI image end-members	0.0000	0.1494	0.0058	0.0025
User selected ROI spectral end-members	0.0001	0.0307	0.0041	0.0025
ASU mineral end-members	0.0000	1.1044	0.0044	0.0030
Ward's whole-rock end-members	0.0000	0.1302	0.0062	0.0054

Based on spectral analysis and the occurrence of specific units associated with crater morphological features such as rim, wall, floor, and central uplift, we can conclude that the pre-impact stratigraphic sequence consisted of: ROI unit 1 ("rim rock") is most likely dolomitic and the topmost unit in the sequence based on its occurrence within the rim. Because of the colors associated with this unit in both the SWIR-MNF and DCS-TIR images (Figs. 2a and 2b), it appears to "surround" Haughton (i.e., as undisturbed unit A) since the ejecta has been subsequently eroded away. ROI unit 1 conformably overlies ROI unit 2 ("wall rock"), which is most likely a quartz-bearing, or cherty, limestone. ROI unit 2's color is consistent with undisturbed target unit B in both

SWIR-MNF and DCS- TIR images (Figs. 2a and 2b). ROI Unit 2 stratigraphically overlies the gypsum-rich ROI unit 3 ("eastern floor"). Though ROI unit 2 and ROI unit 5 ("central uplift") have the same spectral shapes (i.e., composition), they appear to be separated by ROI unit 3. Thus, the final sequence from the topmost (unit 1) exposed lithologies within Haughton to the bottommost (unit 4) is:

- dolomitic rock
- limestone
- gypsum-rich carbonate rock
- limestone

This stratigraphic succession agrees well with the undisturbed target sequence lithologies (units A–C) (Figs. 2a and 2b) The "crater moat" unit is summarized separately below, as it is not believed to be part of either the impact-exposed subsurface stratigraphy or the undisturbed target stratigraphic sequence.

The "Crater Moat" Unit: Fluvial/Glacial or Intra-Crater Deposit?

The unit labeled "crater moat" unit is areally the largest spectral unit within the Haughton impact structure (Fig. 2). This unit is not believed to be part of the impact-exposed subsurface stratigraphy, but probably formed either during the late stages of the impact event (e.g., a breccia or melt sheet unit), or as a post-impact deposit (e.g., fluvial/lacustrine, or glacial). Our preferred interpretation is that the unit represents a polymict breccia, which is based on the following image and spectral observations, which are briefly listed here and the elaborated on below: 1) the unit has spectral similarities in the SWIR and TIR data to the valley-fill and shoreline materials north of the impact structure, but is spectrally distinct from the fill and shoreline deposits in the VNIR; 2) the unit predominately occurs in association with the lining of the crater floor and overlying parts of the crater rim/terraces; and 3) the average "crater moat" ROI spectrum indicates that the unit can be as a mixture of the primary, impact-exposed subsurface lithologies sampled by the impact event.

The "crater moat" unit's spectral distinctness in VNIR from any other unit or deposit in the vicinity of Haughton and its presence predominantly within the Haughton structure are crucial observations that suggest a connection with the impact process. This unit's white, blue-white, and gray-blue coloration as seen in visible and VNIR composite ETM+ and ASTER images, in addition to its distinct low DN values in ETM+ band-ratio images (Figs. 3a and 3b), strongly contrast with the appearance of the other units within and in the vicinity of the Haughton structure. This includes the deposits to the north of Haughton that appear spectrally similar in both the SWIR-MNF and TIR-DCS images (Fig. 2). Because this unit mainly lines the inner topographic depression of Haughton and overlies limestone and dolomites interpreted as part of the "wall/terrace blocks" and "rim," it does not appear to be a part of the subsurface stratigraphy exposed by the crater. As noted earlier, the average spectrum of the "crater moat" unit is believed to be a mixture of the impact-exposed subsurface units based on the positions of absorption features and an overall diminished spectral contrast. Both of these characteristics are consistent with a polymict breccia interpretation. In addition to diminished contrast from mixing, we propose that the low spectral contrast of the "crater moat" unit may also be the result of particle size effects from fine-grained materials (e.g., Moersch and Christensen 1995; Mustard and Hays 1997), presumably the result of strong shock deformation and comminution. Particle size effects may also explain why the "crater moat" unit bears some spectral similarities to the valley-fill and shoreline materials north of the impact structure in the SWIR and TIR (areas that are dark blue and pink in Figs. 2a and 2b, respectively). From the spatial/photogeologic context of these valley-fill and shoreline materials, we speculate that they are also dominated by fine-grain sediments, in this case either fluvially or glacially-derived. Overall, the salient observation with respect to mapping the impact-exposed subsurface lithologies of Haughton is that this unit can be reasonably ruled out as a subsurface unit regardless of its mode of origin.

In summary, our preferred interpretation of this unit, based on photogeologic, morphologic and spectral characteristics, is that the unit represents a polymict breccia composed predominantly of carbonate with an admixture of silicate (quartz-rich component) and potentially sulfate components (gypsum).

Deconvolution Results and Interpretations

Table 4 provides the root mean square (RMS) errors for the deconvolution/unmixing analyses via least-squares fit to the ASTER TIR image spectra using the four end-member libraries (i.e., PPI, ROI, mineral, and rock). As can be seen by the relatively low RMS errors, the four end-member libraries were sufficient to unmix the ASTER TIR image spectra.

The whole-image deconvolution results using the whole-rock (Ward's) library end-members are all presented in Figs. 6a–e. These results clearly define the same spectral units defined by the mapping techniques applied above (compare Figs. 6a–d with Figs. 2a–d). These newly defined units in Figs. 6a–d are directly related to compositions, and are consistent with the interpretations and the spectral results for the ROI spectral units discussed above. Fig. 6a is the deconvolution image for the Ward's end-member "rock gypsum." High concentrations of gypsum occur in the unit defined as ROI unit 3 ("eastern floor") and also outside of Haughton in the undisturbed unit C (cf. Figs. 2a and 2b). Fig. 6b is the deconvolution image for the Ward's end-member "dolomitic limestone." The highest concentration of this end-member appears to be associated with ROI unit 1 ("rim rock") and the undisturbed unit A. Fig. 6c is the deconvolution image for the Ward's end-member "cherty limestone," with major occurrences of this particular end-

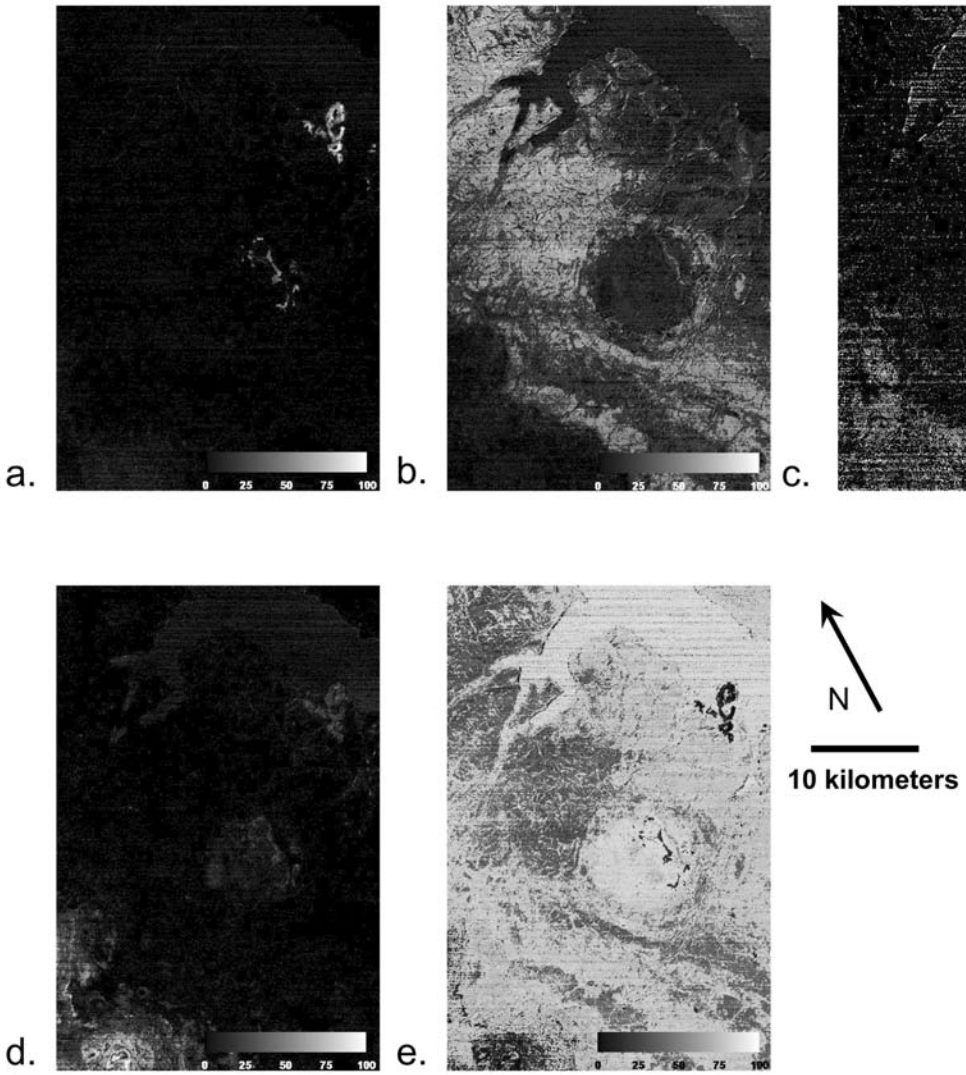

Fig. 6. Whole-image deconvolution of a subset of the ASTER scene covering the Haughton impact structure and surrounding area. Black and white color ramp/scale numbers represent the percentage of end-member present in each pixel. a) Rock gypsum end-member image. b) Dolomitic limestone end-member image. c) Cherty limestone end-member image. d) Siltstone end-member image. e) Blackbody end-member image. In all cases, bright areas indicate higher concentrations of the appropriate end-member.

member concentrated within the crater wall/terraces and in the centrally uplifted blocks within Haughton (i.e., crater ROI unit 2 and unit 4, respectively) (Fig. 2). Undisturbed outcrops of limestone can also be seen to the east (unit B) (Figs. 2a and 2b) and west of Haughton. Fig. 6d is the deconvolution image for the end-member "siltstone" or "shale" (both end-members produced similar results). This component appears in the whole-image deconvolution results within some of the pixels associated with the "crater moat" unit and in outcrops of gypsum both within and outside of Haughton. The brightest pixels representing outcrops to the west of Haughton (i.e., up the stratigraphic section and not affected by the Haughton impact event) are beds of siltstone/shale. The occurrence of some pixels associated with ROI unit 3 ("eastern floor") are probably due to some spectral contributions from quartz. Fig. 5e represents the abundances for the blackbody end-member, with the brightest areas being regions that are best approximated by a blackbody. Water has a near-blackbody TIR spectrum; therefore, the entire area to the ENE in Fig. 5e that is brightest is interpreted as a body of water and ice (confirmed in VNIR imagery). The next-brightest group of pixels in the blackbody deconvolution image occurs within the crater floor of Haughton, suggesting that the ROI unit 4 ("crater moat") also approximates a blackbody (i.e., has very low spectral contrast).

Ground Truth: Comparison of Results and Interpretations with the Geologic Map and Past Field Studies of Haughton

A first order attempt to ground-truth our results was made by comparing spectral units defined in SWIR-MNF

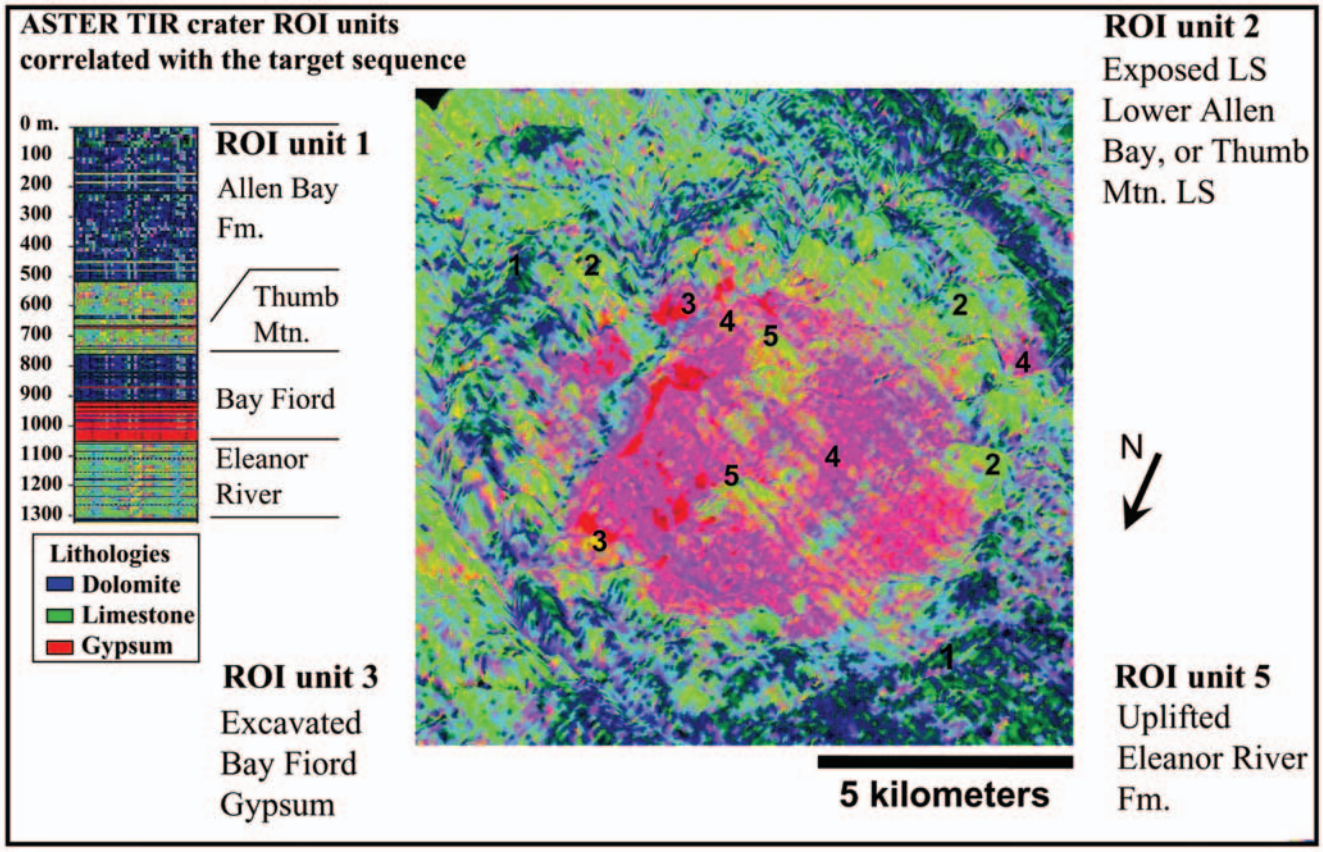

Fig. 7. Lithologic map and stratigraphic column as interpreted from the combined results from the spectral analysis and by comparing both the geologic map and stratigraphic column from Fig. 1 with the ASTER TIR band 14, 12, 10 DCS image draped over the 25 m resolution DEM. Numbered areas on the image represent the respective crater ROI unit numbers, with increasing numbers corresponding to increasing stratigraphic/excavation depth. Dark blue-green ROI unit 1 ("rim rock") = dolomite from the Middle Member of the Allen Bay Formation; yellow-green crater ROI unit 2 ("wall rock") = limestones of the lower member Allen Bay and Thumb Mountain (Mtn.) Formation (pre-impact depth of 500 and 700 m, respectively); red crater ROI unit 3 ("eastern floor") = gypsum from the Bay Fiord Formation (pre-impact depth of ~1000 m); and yellow-green crater ROI unit 5 ("central uplift") = cherty limestone from the Eleanor River Formation (pre-impact depth range of ~1100 m). The pink crater ROI unit 4 ("crater moat") unequivocally corresponds to the Haughton impact melt breccia unit as mapped in the field. The DEM was provided by Natural Resources of Canada; the vertical exaggeration was set to 10×.

(Figs. 2a and 2c), TIR-DCS (Figs. 2b and 2d), ETM+ band ratio (Figs. 3a and 3b), and Ward's end-member concentration images (Figs. 6a–d) with the lithologic units defined in the geologic map and reconstructed stratcolumn by Osinski (2004) and Osinski et al. (2005a), modified after Thorsteinsson and Mayr (1987) (Figs. 1a and 1b; map insert). Crater ROI units identified in the SWIR-MNF and TIR-DCS images (Fig. 2) were directly correlated with mapped lithologies from depth (i.e., further down the pre-impact stratigraphic target sequence; units A–C). Fig. 7 shows a simplified stratigraphic column and a labeled version of the TIR-DCS image draped over the 25 m resolution DEM (obtained from Natural Resources of Canada). Other combinations of bands from both ASTER and ETM+ show similar spatial correlations, but we present the column derived from the ASTER TIR emissivity bands because 1) these data are the best analog for the Mars Odyssey THEMIS; and 2) the ASTER TIR emissivity product was the only data set used in this study that was capable of a full spectral analysis. Correlations between the crater ROI units with the field map and stratigraphic column are summarized below:

1. ROI unit 1 ("rim rock") is directly correlated with the Middle Member of the Allen Bay Formation, which consists predominantly of dolomite. Unit A is the surface exposure of the Middle Member of the Allen Bay Formation outside of the crater (Figs. 2a and 2b).
2. ROI unit 2 ("wall rock"), in the context of the Haughton geologic map, is interpreted as exposed wall rock and slumped terrace blocks of the Lower Member of the Allen Bay Formation and Thumb Mountain Formation. These exposed formations consist predominantly of limestones from a pre-impact depth of 500 to 750 m. Due to the regional tilt of ~3–5° to the WSW, limestones of the Lower Member Allen Bay Formation and the Thumb Mountain Formation (Unit B) are observable in Figs. 2a and 2b and conformably underlie

the dolomites of the Middle Member Allen Bay Formation (unit A).

3. ROI unit 3 ("eastern floor") is mapped as bright red gypsum-rich layers that outcrop from underneath the eroded impact melt breccia unit incised by the Haughton River. The gypsum of ROI unit 3 unequivocally corresponds to Member A of the Bay Fiord Formation that occurred at a depth of ~1000 m in the pre-impact target sequence. Isolated spots of gypsum within the impact melt breccias are interpreted as megablocks of Bay Fiord Formation, but several could be post-impact hydrothermal deposits (Osinski et al. 2001, 2005a). Outcrops of undisturbed gypsum-rich Bay Fiord Formation can be observed just at the eastern edge of our scene as bright red unit C (Fig. 2b).
4. ROI Unit 4 ("crater moat") corresponds to the impact melt breccia unit as observed in the field, proving that this unit is indeed an impact-related unit and not a coherent subsurface unit exposed by the impact process.
5. ROI Unit 5 ("central uplift") is interpreted as uplifted limestones of the Eleanor River Formation based on field studies and its occurrence in the central uplift (Bischoff and Oskierski 1988; Osinski and Spray 2005). The minimum pre-impact depth of the Eleanor River Formation is ~1100 m. Unfortunately, no well-defined exposures of undisturbed outcrops of Eleanor River Formation could be found in our ASTER scene to compare with the central uplift occurrence of this unit.

Ground Truth: Comparison of Image-Derived Spectra with Haughton Sample Spectra

Further ground truth of our results was provided by comparing laboratory thermal emission spectra of whole-rock samples from Haughton to the PPI-IEM spectra (Figs. 5a–e). We compared the PPI-IEMs instead of the ROI-averaged spectra, because the PPI-IEMs theoretically represent pure end-members (i.e., they are analogous to a freshly extracted sample from an outcrop, but at a 90 m scale), whereas the ROI-averaged spectra would represent an average of fresh, weathered, and altered surfaces. The Haughton whole-rock sample spectra were collected using a Nicolet Nexus 670 spectrometer at Arizona State University, as described in detail by Ruff et al. (1997).

Table 5 lists the samples used in this study and their relative compositions based on qualitative analyses from the X-ray diffraction (XRD) method of sample powders, or semi-quantitative analyses using an energy-dispersive spectral analysis (EDS) method (Osinski 2004). Fig. 8 compares the lab spectra of these samples (convolved to the ASTER spectral resolution) with the PPI-IEM spectra. ROI-averaged spectra were matched to PPI-IEM spectra. By this association we can link the laboratory spectra of field samples to the proper ROI-averaged spectra as well. Comparison of the spectra plotted in Fig. 8 confirms both our blind and field-based interpretations. Observations and interpretations from Fig. 8 are summarized below:

Table 5. Qualitative and semi-quantitative compositions of samples from Haughton and surrounding country rock.

Samples	Formation	Mineral composition
02-035	Bay Fiord	Gypsum and anhydrite
00-031	Middle Allen Bay	Dolomite with minor calcite and quartz
00-050	Lower Allen Bay	Calcite with minor dolomite and quartz
00-035	Haughton impact-melt breccia	~28 vol% calcite groundmass
		~25 vol% glass groundmass
		~47 vol% clasts
		dolomite >> limestone, sandstone, shale, crystalline basement

1. PPI-IEM#1 (matched to ROI unit 3) has the same overall spectral shape and major absorption feature (Fig. 8a) as the spectrum for a hand specimen of gypsum collected from the Bay Fiord Formation (sample #02-035).
2. PPI-IEM#2 (matched to ROI unit 1) has a major absorption feature (Fig. 8b) that is congruent with the major absorption feature in the spectrum of dolomite from the Middle Member Allen Bay Formation (sample #00-031). The differences that can be seen between the sample spectrum and the spectrum of PPI-IEM#2 (around 8.63 μm and 9.08 μm) are likely from spectral contributions that arise from the addition of quartz, phyllosilicates, and/or gypsum.
3. PPI-IEM#3 (matched to ROI unit 2 and unit 5) appears to have spectral contributions from additional quartz, phyllosilicates, and/or gypsum, as does the sample of limestone from the Lower Member Allen Bay Formation (sample #00-050). The same overall spectral shape suggests a good match despite an offset in spectral contrast. Due to ASTER spectral resolution, limestone from any formation (e.g., from the Lower Member Allen Bay and Eleanor River formations) cannot be spectrally distinguished from another.
4. Although lacking a stronger absorption at 9.08 μm, the spectrum for PPI-IEM#5 (matched to ROI unit 4 "crater moat") is a sufficient match for the spectrum of a sample collected from Haughton's impact melt breccia unit (sample #00-035). The stronger absorption in the PPI-IEM spectrum at 9.08 μm suggests that quartz is more abundant in this end-member at a 90 m/pixel scale. This stronger absorption is likely to arise from a mixture of the breccia unit and surface deposits that are likely to be rich in weather-resistant quartz.

Applications to Mars

While the utility of TIR and SWIR remote sensing for mapping the surface composition of Mars is generally recognized, our work on the Haughton impact structure

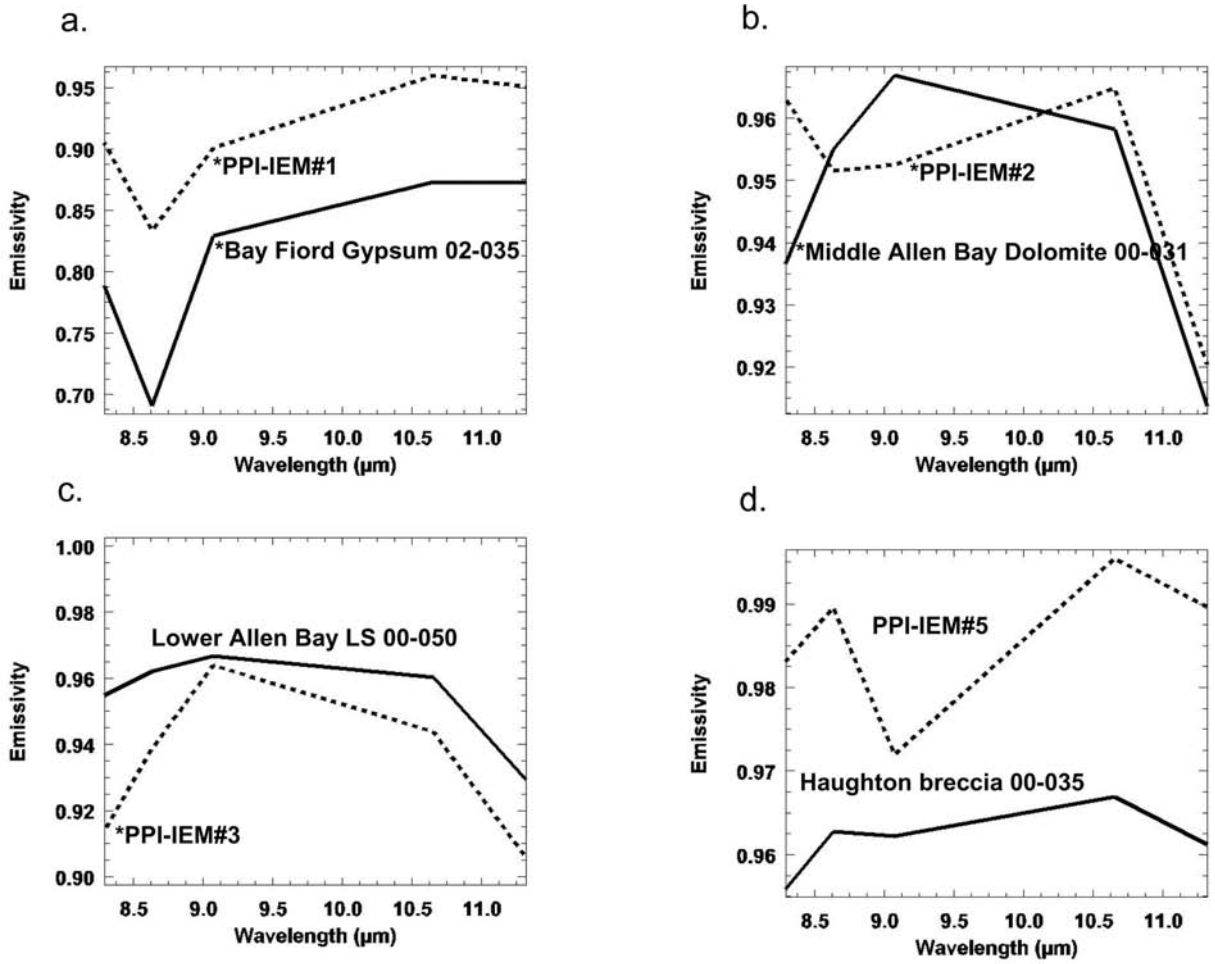

Fig. 8. Laboratory-measured thermal infrared spectra of Haughton whole-rock samples convolved to ASTER TIR band passes comparison to image-derived end-member spectra (PPI-IEMs) from the ASTER TIR emissivity data product. a) A plot of the average spectrum for PPI-IEM#1 and a sample spectrum of gypsum from the Bay Fiord Formation (sample #02-035). b) A plot of the average spectrum for PPI-IEM#2 and a sample spectrum of dolomite from the Middle Member Allen Bay Formation (sample #00-031). c) A plot of the average spectrum for PPI-IEM#3 and a sample spectrum of limestone from the Lower Member Allen Bay Formation (sample #00-050). d) The average spectrum for PPI-IEM#5 and a sample spectrum of an allochthonous impact melt breccia (sample 00-035).

suggests that it may also be possible to make inferences about Martian subsurface geology via impact craters. In addition to stratigraphy, an understanding of subsurface and shallow crust mineral chemistry based on compositional mapping of materials exhumed in Martian impact craters would give important additional insight into the petrogenetic and geologic history of the Martian crust (Tornabene 2003).

Recent discoveries of extensive layering exposed across much of the planet (Malin and Edgett 2000; Edgett and Malin 2002) imply that significant vertical inhomogeneities may exist in the Martian crust. Further direct evidence for compositional variation in the Martian surface layer comes from the results of the MGS-TES instrument, which suggests that there are heterogeneities at a coarse (~3 × 6 km/pixel) spatial resolution (Bandfield et al. 2000; Christensen et al. 2001a, 2001b, 2004; Wyatt and McSween 2002; Hamilton et al. 2003; Hoefen et al. 2003; Morris et al. 2004). TES data reveals two spectral surface regions on a global scale, surface type 1 and surface type 2, which are generally divided along the Martian crustal dichotomy boundary (Bandfield et al. 2000; Christensen et al. 2000b). The surface type 1 spectrum is interpreted to represent a basaltic composition, whereas the spectrum of surface type 2 has been variously interpreted as basaltic andesite-andesite (Bandfield et al. 2000b) or weathered basalt (Wyatt and McSween 2002). Despite the dispute over the interpretation of surface type 2, basaltic outliers have been observed in the northern lowlands (Rogers and Christensen 2003), but these are rare at TES resolutions and by no means favors one interpretation over the other. A study of crater-excavated materials along the Martian dichotomy boundary at THEMIS resolutions (100 m/pixel) may provide some insight on a possible stratigraphic relationship between these two global units or even constrain the interpretation of this surface unit.

At regional scales, the Mars orbiter camera (MOC) on Mars Global Surveyor has imaged layering throughout the planet (Malin and Edgett 2000; Edgett and Malin 2002), possibly suggesting petrologic and compositional variations at a local scale. Subsurface layers of sulfate-rich siliciclastic sedimentary rocks exposed by small craters were recently imaged and analyzed in situ by the Opportunity Rover. These outcropping bedrocks occur in the crater wall of the Eagle crater (20 m in diameter), the Fram crater (9 m in diameter), and the Endurance crater (152 m in diameter) in Meridiani Planum (Squyres et al. 2004). These examples demonstrate a need for subsurface lithologic mapping on Mars in order to understand the petrogenesis and geologic history of the Martian crust at even regional scales. This includes any available means to more directly determine subsurface geology such as a remote sensing study of impact-exposed, excavated, or uplifted materials. These studies may tell us much about these subsurface compositions in areas where layers are not otherwise exposed at the surface (e.g., within valles or fossae).

Despite the success of our terrestrial example presented here, Mars brings additional challenges that could make identification and mapping of crater spectral units difficult. In particular, dust and soils on Mars obscure much of the planet's bedrock geology, hampering spectral measurements, especially at regional scales (Johnson et al. 2002c; Ruff and Christensen 2002). Nevertheless, areas with low enough dust cover could allow identification of surface compositions [e.g., (Bandfield et al. 2000)]. Mapping of subsurface compositions exhumed by Martian impact craters may also prove more challenging than the Haughton example, because the spectra of typical Martian compositions (e.g., surface types 1 and 2) are not as spectrally distinct as the spectra of the lithologies at Haughton (i.e., carbonates, sulfates, and siliclastics). However, THEMIS does enjoy some advantages over ASTER for compositional mapping of the surface, which may partially mitigate some of these challenges. THEMIS has access to more of the TIR spectral range than is available to any Earth-orbiting TIR spectrometer, because the Martian atmospheric transparency window is somewhat wider (cf. THEMIS and ASTER in Table 1). THEMIS also makes use of eight bands that image the surface, as opposed to ASTER's five, which improves the potential for proper identification and unmixing of spectra.

SUMMARY AND CONLUSIONS

Without the aid of a geologic field map or stratigraphic column, most of the major units sampled and exposed by the Haughton impact event can be identified and mapped by remote sensing techniques alone. The lithologies exposed, excavated or uplifted within the 23 km (apparent) diameter Haughton impact structure can be spectrally and, via interpretation, lithologically mapped using simple spectral processing techniques. The regional tilt of the impacted stratigraphy in the vicinity of Haughton conveniently offers the means to compare the lithologies exposed by the crater with an undisturbed target stratigraphic sequence just to the west of the crater. This comparison allowed the succession of undisturbed units A–C (Figs. 2a and 2b) to be directly correlated with the progression of the manually defined crater morphologic/spectral regions of interest (ROIs). The average spectra for crater ROI units and pixel purity indexed (PPI) and n-dimensional visualizer extracted image end-members (PPI-IEMs) were successfully matched to both mineral (ASU) and whole-rock (Ward's) spectral library end-members. Based on the spectral matching and the defined crater ROI units, a sequence of units was determined progressing from the shallowest subsurface unit exposed within the rim to the deepest exposed unit within the central uplift:

- dolomitic limestone in the "rim"
- limestone in the wall/terraces
- gypsum-rich carbonate (eastern floor)
- limestone in the central uplift

This distribution of the resulting spectral/lithologic units from the processed remote sensing images compares very well with the most recent geologic map and pre-impact stratigraphic sequence of Haughton (Fig. 1; map insert). Ground truth was provided by comparing TIR-acquired spectra of well-characterized Haughton hand specimens with the spectra extracted from the ASTER scene. These comparisons corroborate our interpretations of the remote data.

The use of craters as a means to map subsurface lithologies and stratigraphy by remote spectroscopic studies is demonstrated here. If the regional tilt of the target sequence was significantly less or nearly zero, Haughton would be completely surrounded by the dolomite of the Middle Member Allen Bay Formation with the only subsurface exposure being within valleys and within the excavated and uplifted target materials outcropping within the crater as a natural "window" into the crust. By using ASTER and Landsat ETM+ data as analogs for Mars remote sensing instruments, this study serves as a terrestrial proof-of-concept that subsurface geology of Mars may be successfully mapped on Mars via moderately to well-preserved impact craters that are not obscured by dust or surface deposits. Because tectonics is less pervasive on Mars than Earth, impact craters provide the most convenient means to locate, map, and identify the diverse mineral and lithologic compositions of Martian crust.

Acknowledgments–We would like to thank NASA's Haughton-Mars Project for infrastructure and field data that was invaluable to this study. We would like to acknowledge Carol Stoker of NASA Ames Research Center for providing the Landsat 7 ETM+ data. We appreciate Jen Piatek for translating Mike Ramsey's deconvolution code from FORTRAN to IDL/ENVI. Brandy Adams was especially helpful in facilitating the acquisition and data product processing of the ASTER level 1A and 1B data sets. We

would also like to acknowledge David Wettergreen of Carnegie Mellon University and Natural Resources of Canada for the 100-meter and 25-meter DEMs of the Haughton structure that were used in this study. We would like to extend a special thanks to Bill Farrand, Thomas H. Burbine Jr. and one anonymous reviewer for their thorough, insightful and constructive reviews of this manuscript.

Editorial Handling—Dr. Wolf Uwe Reimold

REFERENCES

Abrams M. 2000. The Advanced Spaceborne Thermal Emission and Reflection Radiometer (ASTER): Data products for the high spatial resolution imager on NASA's Terra platform. *International Journal of Remote Sensing* 21:847–859.

Adams J. B., Smith M. O., and Gillespie A. R. 1993. Imaging spectroscopy: Interpretation based on spectral mixture analysis. In *Remote geochemical analysis: Elemental and mineralogical composition*, edited by Pieters C. and Englert P. Cambridge: Cambridge University Press. pp. 145–166.

Bandfield J. L., Hamilton V. E., and Christensen P. R. 2000. A global view of the martian surface compositions from MGS-TES. *Science* 287:1626–1630.

Bandfield J. L., Hamilton V. E., Christensen P. R., and McSween H. Y. 2004. Identification of quartzofeldspathic materials on Mars. *Journal of Geophysical Research* 109:E10.

Bibring J. P., Langevin Y., Gendrin A., Gondet B., Poulet F., Berthe M., Soufflot A., Arvidson R., Mangold N., Mustard J., and Drossart P. 2005. Mars surface diversity as revealed by the OMEGA/Mars Express observations. *Science* 307:1576–1581.

Bischoff L. and Oskierski W. 1988. The surface structure of the Haughton impact crater, Devon Island, Canada. *Meteoritics & Planetary Science* 23:209–220.

Boardman J. W. and Kruse F. A. 1994. Automated spectral analysis: A geological example using AVIRIS data, north Grapevine Mountains, Nevada. Proceedings, ERIM 10th Thematic Conference on Geologic Remote Sensing. pp. I-407–I-418.

Boardman J. W., Kruse F. A., and Green R. O. 1995. Mapping target signatures via partial unmixing of AVIRIS data. Proceedings, 5th JPL Airborne Earth Science Workshop. pp. 23–26.

Chavez P. S. 1988. An improved dark-object subtraction technique for atmospheric scattering correction of multispectral data. *Remote Sensing of the Environment* 24:459–479.

Christensen P. R., Anderson D. L., Chase S. C., Clark R. N., Kieffer H. H., Malin M. C., Pearl J. C., Carpenter J., Bandiera N., Brown F. G., and Silverman S. 1992. Thermal emission spectrometer experiment—Mars Observer mission. *Journal of Geophysical Research* 97:7719–7734.

Christensen P. R., Anderson D. L., Chase S. C., Clancy R. T., Clark R. N., Conrath B. J., Kieffer H. H., Kuzmin R. O., Malin M. C., Pearl J. C., Roush T. L., and Smith M. D. 1998. Results from the Mars Global Surveyor thermal emission spectrometer. *Science* 279:1692–1698.

Christensen P. R., Jakosky B. M., Kieffer H. H., Malin M. C., Nealson K., McSween H. Y. Jr., Mehall G. L., Silverman S., and Ferry S. 1999. The Thermal Emission Imaging System (THEMIS) instrument for the Mars 2001 Orbiter (abstract #1470). 30th Lunar and Planetary Science Conference. CD-ROM.

Christensen P. R., Bandfield J. L., Hamilton V. E., Howard D. A., Lane M. D., Piatek J. L., Ruff S. W., and Stefanov W. L. 2000a. A thermal emission spectral library of rock-forming minerals. *Journal of Geophysical Research* 105:9735–9739.

Christensen P. R., Bandfield J. L., Smith M. D., Hamilton V. E., and Clark R. N. 2000b. Identification of a basaltic component on the Martian surface from thermal emission spectrometer data. *Journal of Geophysical Research* 105:9609–9621.

Christensen P. R., Bandfield J. L., Hamilton V. E., Ruff S. W., Kieffer H. H., Titus T. N., Malin M. C., Morris R. V., Lane M. D., Clark R. L., Jakosky B. M., Mellon M. T., Pearl J. C., Conrath B. J., Smith M. D., Clancy R. T., Kuzmin R. O., Roush T., Mehall G. L., Gorelick N., Bender K., Murray K., Dason S., Greene E., Silverman S., and Greenfield M. 2001a. Mars Global Surveyor thermal emission spectrometer experiment: Investigation description and surface science results. *Journal of Geophysical Research* 106:23,823–23,871.

Christensen P. R., Morris R. V., Lane M. D., Bandfield J. L. and Malin M. C. 2001b. Global mapping of Martian hematite mineral deposits: Remnants of water-driven processes on early Mars. *Journal of Geophysical Research* 106:23,873–23,885.

Christensen P. R., Bandfield J. L., Bell J. F., Gorelick N., Hamilton V. E., Ivanov A., Jakosky B. M., Kieffer H. H., Lane M. D., Malin M. C., McConnochie T., McEwen A. S., McSween H. Y., Mehall G. L., Moersch J. E., Nealson K. H., Rice J. W., Richardson M. I., Ruff S. W., Smith M. D., Titus T. N., and Wyatt M. B. 2003. Morphology and composition of the surface of Mars: Mars Odyssey THEMIS results. *Science* 300:2056–2061.

Christensen P. R., Jakosky B., Kieffer H. H., Malin M. C., McSween H. Y., Nealson K., Mehall G. L., Silverman S. H., Ferry S., Caplinger M. and Ravine M. 2004. The Thermal Emission Imaging System (THEMIS) for the Mars 2001 Odyssey Mission. *Space Science Reviews* 110:85–130.

Dence M. R. 1972. The nature and significance of terrestrial impact structures. Proceedings, International Geological Congress: Planetology. pp. 77–89.

Drury S. A. 2001. *Image interpretation in geology*, 3rd ed. Malden: Blackwell Science. 290 p.

Edgett K. S. and Malin M. C. 2002. Martian sedimentary rock stratigraphy: Outcrops and interbedded craters of northwest Sinus Meridiani and southwest Arabia Terra. *Geophysical Research Letters* 29, doi:10.1029/2002GL016515.

Frisch T. and Thorsteinsson R. 1978. Haughton-Astrobleme-Mid-Cenozoic Impact Crater Devon Island, Canadian Arctic Archipelago. *Arctic* 31:108–124.

Garvin J. B., Schnetzler C. C., and Grieve R. A. F. 1992. Characteristics of large terrestrial impact structures as revealed by remote-sensing studies. *Tectonophysics* 216:45–62.

Gillespie A. R., Kahle A. B., and Walker R. E. 1986. Color enhancement of highly correlated images. 1. Decorrelation and HSI Contrast Stretches. *Remote Sensing of Environment* 20:209–235.

Goward S. N., Masek J. G., Williams D. L., Irons J. R., and Thompson R. J. 2001. The Landsat 7 mission—Terrestrial research and applications for the 21st century. *Remote Sensing of the Environment* 78:3–12.

Green A. A., Berman M., Switzer P., and Craig M. D. 1988. A transformation for ordering multispectral data in terms of image quality with implications for noise removal. *IEEE Transactions on Geoscience and Remote Sensing* 26:65–74.

Greiner H. R. 1963. Haughton Dome and area southwest of Thomas Lee Inlet. In *Geology of the north-central part of the Arctic Archipelago, Northwest Territories (Operation Franklin)*. Geological Survey of Canada Memoir #320, edited by Fortier Y. O., Blackadar R. G., Glenister B. F., Greiner H. R., McLaren D. J., McMillan N. J., Norris A. W., Roots Souther J. G., Thorsteinsson R., and Tozer E. T. Ottawa: Geological Survey of Canada. pp. 208–216.

Grieve R. A. F., Robertson P. B., and Dence M. R. 1981. Multi-ring basins: Formation and evolution. Proceedings, 12th Lunar and Planetary Science Conference. pp. 791–814.

Grieve R. A. F. and Pilkington M. 1996. The signature of terrestrial impacts. *AGSO Journal of Australian Geology and Geophysics* 16:399–420.

Grieve R. A. F. and Therriault A. M. 2004. Observations at terrestrial impact structures: Their utility in constraining crater formation. *Meteoritics & Planetary Science* 39:199–216.

Hajnal Z., Scott D., and Robertson P. B. 1988. Reflection study of the Haughton Impact Crater. *Journal of Geophysical Research* 93: 11,930–11,942.

Hamilton V. E., Christensen P. R., McSween H. Y., and Bandfield J. L. 2003. Searching for the source regions of martian meteorites using MGS TES: Integrating martian meteorites into the global distribution of igneous materials on Mars. *Meteoritics & Planetary Science* 38:871–885.

Hamilton V. E. and Christensen P. R. 2005. Evidence for extensive, olivine-rich bedrock on Mars. *Geology* 33:433–436.

Hickey L. J., Johnson K. R., and Dawson M. R. 1988. The stratigraphy, sedimentology, and fossils of the Haughton Formation–A post-impact crater-fill, Devon Island, NWT, Canada. *Meteoritics* 23:221–231.

Hoefen T. M., Clark R. N., Bandfield J. L., Smith M. D., Pearl J. C., and Christensen P. R. 2003. Discovery of olivine in the Nili Fossae region of Mars. *Science* 302:627–630.

Housen K. R., Schmidt R. M., and Holsapple K. A. 1983. Crater ejecta scaling laws—Fundamental forms based on dimensional analysis. *Journal of Geophysical Research* 88:2485–2499.

Jessberger E. K. 1988. Ar-40-Ar-39 dating of the Haughton Impact Structure. *Meteoritics* 23:233–234.

Johnson J. R., Hörz F., Lucey P. G., and Christensen P. R. 2002a. Thermal infrared spectroscopy of experimentally shocked anorthosite and pyroxenite: Implications for remote sensing of Mars. *Journal of Geophysical Research* 107, doi:10.1029/2001JE001517, 2002.

Johnson J. R., Staid M. I., and Titus T. N. 2002b. Shocked plagioclase signatures in thermal emission spectrometer data of Mars (abstract #1345). 33rd Lunar and Planetary Science Conference. CD-ROM.

Johnson J. R., Christensen P. R., and Lucey P. G. 2002c. Dust coatings on basaltic rocks and implications for thermal infrared spectroscopy of Mars. *Journal of Geophysical Research* 107, doi: 10.1029/2000JE001405.

Johnson J. R., Hörz F., and Staid M. I. 2003. Thermal infrared spectroscopy and modeling of experimentally shocked plagioclase feldspars. *American Mineralogist* 88:1575–1582.

Johnson J. R. and Hörz F. 2003. Visible/near-infrared spectra of experimentally shocked plagioclase feldspars. *Journal of Geophysical Research* 108, doi:10.1029/2003JE002127.

Kruse F. A., Lefkoff A. B., Boardman J. W., Heidebrecht K. B., Shapiro A. T., Barloon P. J., and Goetz A. F. H. 1993. The spectral image-processing system (Sips)—Interactive visualization and analysis of imaging spectrometer data. *Remote Sensing of the Environment* 44:145–163.

Lana C., Gibson R. L., and Reimold W. U. 2003a. Central uplift formation in very large impact structures: Evidence from the Vredefort dome (abstract #1009). 34th Lunar and Planetary Science Conference. CD-ROM.

Lana C., Gibson R. L., and Reimold W. U. 2003b. Impact tectonics in the core of the Vredefort dome, South Africa: Implications for central uplift formation in very large impact structures. *Meteoritics & Planetary Science* 38:1093–1107.

Lee P. and Osinski G. R. 2005. Intra-crater sedimentary deposits at the Haughton impact structure, Devon Island, Canadian High Arctic. *Meteoritics & Planetary Science* 40. This issue.

Malin M. C. and Edgett K. S. 2000. Sedimentary rocks of early Mars. *Science* 290:1927–1937.

Melosh H. J. 1989. *Impact cratering: A geologic process*. New York: Oxford University Press. 245 p.

Moersch J. E. and Christensen P. R. 1995. Thermal emission from particulate surfaces–A comparison of scattering models with measured spectra. *Journal of Geophysical Research* 100:7465–7477.

Morris R. V., Graff T. G., Ming D. W., Bell J. F. I., Le L., Mertzman S. A., and Christensen P. R. 2004. Palagonitic Mars: A basalt centric view of surface composition and aqueous alteration (abstract # 1606). 35th Lunar and Planetary Science Conference. CD-ROM.

Murchie S., Arvidson R., Beisser K., Bibring J. P., Bishop J., Boldt J., Bussey B., Choo T., Clancy R. T., Darlington E. H., Des Marais D., Fasold M., Fort D., Green R., Guiness E., Hayes J., Heyler G., Humm D., Lee R., Lees J., Lohr D., Malaret E., Morris R., Mustard J., Rhodes E., Robinson M., Roush T., Schaefer E., Seagrave G., Silvergate P., Smith M., Strohbehn K., Thompson P., and Tossman B. 2003. CRISM: Compact reconnaissance imaging spectrometer for Mars on the Mars Reconnaissance Orbiter (abstract #3062). Proceedings, 6th International Conference on Mars. CD-ROM.

Mustard J. F. and Hays J. E. 1997. Effects of hyperfine particles on reflectance spectra from 0.3 to 25 mu m. *Icarus* 125:145–163.

Osinski G. R., Spray J. G., and Lee P. 2001. Impact-induced hydrothermal activity within the Haughton impact structure, arctic Canada: Generation of a transient, warm, wet oasis. *Meteoritics & Planetary Science* 36:731–745.

Osinski G. R. 2004. Impacts into sedimentary targets: Constraints from the Haughton and Ries impact structures. Ph.D. thesis, University of New Brunswick, Fredericton, New Brunswick, Canada.

Osinski G. R., Lee P., Spray J. G., Parnell J., Lim D. S. S., Bunch T. E., Cockell C. S. and Glass B. 2005a. Geological overview and cratering model for the Haughton impact structure, Devon Island, Canadian High Arctic. *Meteoritics & Planetary Science* 40. This issue.

Osinski G. R., Lee P., Parnell J., Spray J. G., and Baron M. 2005b. A case study of impact-induced hydrothermal activity: The Haughton impact structure, Devon Island, Canadian High Arctic. *Meteoritics & Planetary Science* 40. This issue.

Osinski G. R., Spray J. G., and Lee P. 2005c. Impactites of the Haughton impact structure, Devon Island, Canadian High Arctic. *Meteoritics & Planetary Science* 40. This issue.

Osinski G. R. and Spray J. G. 2005. Tectonics of complex crater formation as revealed by the Haughton impact structure, Devon Island, Canadian High Arctic. *Meteoritics & Planetary Science* 40. This issue.

Pieters C. M. 1982. Copernicus crater central peak: Lunar mountain of a unique composition. *Science* 215:59–61.

Pieters C. M. 1991. Bullialdus: Strengthening the case for lunar plutons. *Geophysical Research Letters* 18:2129–2132.

Pieters C. M., Staid M. I., Fischer E. M., Tompkins S., and He G. 1994. A sharper view of impact craters from Clementine data. *Science* 266:1844–1848.

Pieters C. M., Tompkins S., Head J. W., and Hess P. C. 1997. Mineralogy of the mafic anomaly in the South Pole-Aitken Basin: Implications for excavation of the lunar mantle. *Geophysical Research Letters* 24:1903–1906.

Ramsey M. S. 1996. Quantitative analysis of geological surfaces: A deconvolution algorithm for midinfrared remote sensing data. Ph.D. thesis, Arizona State University, Tempe, Arizona, USA.

Ramsey M. S. 2002. Ejecta distribution patterns at Meteor Crater, Arizona: On the applicability of lithologic end-member deconvolution for spaceborne thermal infrared data of Earth and

Mars. *Journal of Geophysical Research* 107, doi:10.1029/2001JE001827.

Ramsey M. S. and Christensen P. R. 1998. Mineral abundance determination: Quantitative deconvolution of thermal emission spectra. *Journal of Geophysical Research* 103:577–596.

Redeker H. J. and Stöffler D. 1988. The allochthonous polymict breccia layer of the Haughton Impact Crater, Devon Island, Canada. *Meteoritics* 23:185–196.

Robertson P. B. and Mason G. D. 1975. Shatter cones from Haughton Dome, Devon Island, Canada. *Nature* 255:393–394.

Rogers D. and Christensen P. R. 2003. Age relationship of basaltic and andesitic surface compositions on Mars: Analysis of high-resolution TES observations of the northern hemisphere. *Journal of Geophysical Research* 108, doi:10.1029/2002JE001913.

Rowan L. C., Hook S. J., Abrams M. J., and Mars J. C. 2003. Mapping hydrothermally altered rocks at Cuprite, Nevada, using the advanced Spaceborne Thermal Emission and Reflection Radiometer (ASTER), a new satellite-imaging system. *Economic Geology and the Bulletin of the Society of Economic Geologists* 98:1019–1027.

Rowan L. C. and Mars J. C. 2003. Lithologic mapping in the Mountain Pass, California area using Advanced Spaceborne Thermal Emission and Reflection Radiometer (ASTER) data. *Remote Sensing of the Environment* 84:350–366.

Ruff S. W., Christensen P. R., Barbera P. W., and Anderson D. L. 1997. Quantitative thermal emission spectroscopy of minerals: A laboratory technique for measurement and calibration. *Journal of Geophysical Research* 102:14,899–14,913.

Ruff S. W. and Christensen P. R. 2002. Bright and dark regions on Mars: Particle size and mineralogical characteristics based on Thermal Emission Spectrometer data. *Journal of Geophysical Research* 107, doi:10.1029/2001JE001580.

Schmidt R. M. and Housen K. R. 1987. Some recent advances in the scaling of impact and explosion cratering. *International Journal of Impact Engineering* 5:543–560.

Scott D. and Hajnal Z. 1988. Seismic signature of the Haughton structure. *Meteoritics* 23:239–247.

Squyres S. W., Arvidson R. E., Bell J. F., Bruckner J., Cabrol N. A., Calvin W., Carr M. H., Christensen P. R., Clark B. C., Crumpter L., Des Marais D. J., d'Uston C., Economou T., Farmer J., Farrand W., Folkner W., Golombek M., Gorevan S., Grant J. A., Greeley R., Grotzinger J., Haskin L., Herkenhoff K. E., Hviid S., Johnson J., Klingelhofer G., Knoll A. H., Landis G., Lemmon M., Li R., Madsen M. B., Malin M. C., McLennan S. M., McSween H. Y., Ming D. W., Moersch J., Morris R. V., Parker T., Rice J. W., Richter L., Rieder R., Sims M., Smith M., Smith P., Soderblom L. A., Sutlivan R., Wanke H., Wdowiak T., Wolff M., and Yen A. 2004. The Opportunity rover's Athena science investigation at Meridiani Planum, Mars. *Science* 306:1698–1703.

Thomson J. L. and Salisbury J. W. 1993. The midinfrared reflectance of mineral mixtures (7–14 μm). *Remote Sensing of the Environment* 45:1–13.

Thorsteinsson R. and Mayr U. 1987. The sedimentary rocks of Devon Island, Canadian Arctic Archipelago. Geological Survey of Canada Memoir #411. Ottawa: Geological Survey of Canada. 182 p.

Tompkins S. 1998. Composition and structure of the lunar crust (abstract #6029). Proceedings, Workshop on New Views of the Moon I. CD-ROM.

Tornabene L. L. 2003. Composition of the martian crust: Spectral classification of deep-seated and subsurface lithologies in impact craters using MGS-TES and Odyssey-THEMIS (abstract #0609). Proceedings, Martian Crater Consortium VI. CD-ROM.

Wright S. P. 2003. Thermal infrared data analyses of Meteor Crater, Arizona: Implications for Mars spaceborne data from the Thermal Emission Imaging System. M.S. thesis, University of Pittsburgh, Pittsburgh, Pennsylvania, USA.

Wright S. P. and Ramsey M. S. 2003. Spaceborne thermal infrared data analysis of Meteor Crater, Arizona: Analog for THEMIS data of a small impact crater in Syrtis Major (abstract #1495). 34th Lunar and Planetary Science Conference. CD-ROM.

Wyatt M. B. and McSween H. Y. 2002. Spectral evidence for weathered basalt as an alternative to andesite in the northern lowlands of Mars. *Nature* 417:263–266.